

$\mathcal{A}^2\mathcal{SB}$: *Audio-to-Audio Schrödinger Bridges*

Zhifeng Kong*, Kevin J Shih*, Weili Nie, Arash Vahdat, Sang-gil Lee,
João Felipe Santos, Ante Jukić, Rafael Valle, Bryan Catanzaro

NVIDIA

{zkong, kshih}@nvidia.com

ABSTRACT

Real-world audio is often degraded by numerous factors. This work presents an audio restoration model tailored for high-res music at 44.1kHz. Our model, Audio-to-Audio Schrödinger Bridges ($\mathcal{A}^2\mathcal{SB}$), is capable of both bandwidth extension (predicting high-frequency components) and inpainting (re-generating missing segments). Critically, $\mathcal{A}^2\mathcal{SB}$ is end-to-end requiring no vocoder to predict waveform outputs, able to restore hour-long audio inputs, and trained on permissively licensed music data. $\mathcal{A}^2\mathcal{SB}$ is capable of achieving state-of-the-art bandwidth extension and inpainting quality on several out-of-distribution music test sets.

GitHub Page: <https://github.com/NVIDIA/diffusion-audio-restoration>

Checkpoints: https://huggingface.co/nvidia/audio_to_audio_schrodinger_bridge

Demo Website: <https://research.nvidia.com/labs/adlr/A2SB/>

1 INTRODUCTION

Audio signals in the real world may be perturbed due to numerous factors such as recording devices, data compression, and online transferring. For instance, certain recording devices and compression methods may result in low sampling rate, and online transferring may cause a short audio segment to be lost. These problems are usually ill-posed (Narayanaswamy et al., 2021; Moliner et al., 2023) and are usually solved with data-driven generative models. For instance, bandwidth extension methods have been proposed to up-sample the audio (Lee & Han, 2021; Liu et al., 2022; Serrà et al., 2022; Moliner & Välimäki, 2022; Shuai et al., 2023; Yu et al., 2023; Kim et al., 2024; Liu et al., 2024; Ku et al., 2024; Yun et al., 2025), and inpainting methods have been developed to predict segments where audio is missing (Marafioti et al., 2019; 2020; Borsos et al., 2022; Liu et al., 2023b; Moliner & Välimäki, 2023; Asaad et al., 2024).

Many of these methods are task-specific, designed for the speech domain, or trained to only restore the degraded magnitude – which requires an additional vocoder to transform the restored magnitude into a waveform. In this work, we investigate high-res music restoration, a more challenging task than speech restoration in terms of typical bandwidth of speech ($\leq 22.05\text{kHz}$) vs music signals (44.1kHz). We aim to tackle bandwidth extension and inpainting in a single model as in practice it is easier to maintain one model serving multiple tasks. We also aim to build an end-to-end trainable generative model for audio restoration without need of a separate vocoder or a codec. To achieve our goals, we adopt the Schrödinger Bridge framework (De Bortoli et al., 2021; Chen et al., 2021; Liu et al., 2023a; Albergo et al., 2023) as it is suitable for translation tasks where a part of the source and target samples are well aligned. We name our model $\mathcal{A}^2\mathcal{SB}$: *Audio-to-Audio Schrödinger Bridges*.

The first challenge is curating a dataset that is both expansive enough to cover most genres of music of interest and being permissively licensed. To achieve this, we collected and filtered permissively licensed music data from public datasets, leading to 2.3K hours in total. As data quality varies significantly across datasets, we adopt the common pre-training and fine-tuning approach (Ouyang et al., 2022).

*Equal contribution.

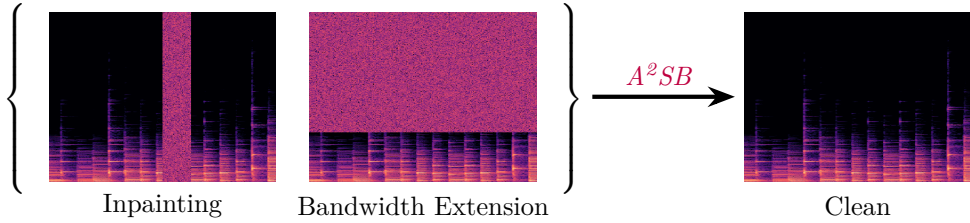


Figure 1: A^2SB targets music restoration with a focus on inpainting and bandwidth extension, each corresponding to a specific corruption pattern in spectrogram. The model is then trained to fit the diffusion Schrödinger Bridge process from the corrupted distribution to the clean distribution.

The second challenge is to support both restoration tasks in a *single* model. We frame both tasks as the generative spectrogram inpainting task: bandwidth extension as inpainting the high-frequency part of the spectrogram along the frequency axis, and audio inpainting as frame inpainting along the time axis. The rest of the spectrogram should exactly match the input. We adopt the Schrödinger Bridge formulation (Liu et al., 2023a; Albergo et al., 2023) as it is particularly suitable for our generative spectrogram inpainting setup.

The third and most significant challenge is to train an *end-to-end* model without using a vocoder or a codec. While prior works such as (Richter et al., 2023; Jukić et al., 2024; Ku et al., 2024) found success training directly on the complex spectrogram for speech enhancement, we find this ineffective when we need to synthesize missing spectrogram data. We use a factorized audio representation with power compression of the magnitude and trigonometric representation of the phase. We additionally apply phase orthogonalization based on the solution of the Procrustes problem to ensure that the generated phase values are consistent. These techniques make A^2SB the first end-to-end high-res music restoration model. It is also advantageous over prior works that restore only the magnitude spectrum and apply a vocoder (Liu et al., 2024; 2023b), as we preserve the original phase values where available.

The fourth challenge is to apply our restoration model – which is trained on a fixed segment length – to very long audio inputs. Directly concatenating individually restored segments could produce boundary artifacts especially for the bandwidth extension task. To solve this problem, we adapt MultiDiffusion (Bar-Tal et al., 2023), which was originally designed for image panorama generation, to our model. We apply MultiDiffusion in overlapping sliding windows along the audio time axis, which allows A^2SB to produce coherently restored outputs for hour-long sequences.

We demonstrate the effectiveness of our A^2SB on several out-of-distribution test sets. Our model outperforms state-of-the-art baselines on these benchmarks. We also demonstrate the effectiveness of our factorized audio representation, phase orthogonalization, and inference methods qualitatively and quantitatively. We summarize our contributions as follows:

1. We propose A^2SB , a state-of-the-art, end-to-end (vocoder-free), and multi-task diffusion Schrödinger Bridge model for 44.1kHz high-res music restoration.
2. We propose an effective factorized audio representation and a phase orthogonalization method to achieve end-to-end training and generation.
3. We curate a large collection of permissively licensed public datasets for high-res music restoration, and design a training strategy for better utilization of the data.
4. A^2SB can coherently restore hour-long audio without boundary artifacts.

2 RELATED WORKS

2.1 DIFFUSION MODELS

Diffusion models and score-based generative models (Sohl-Dickstein et al., 2015; Ho et al., 2020; Song et al., 2021) are a type of generative models that aim to learn the data distribution p_{data} from data

Table 1: Comparison between our A^2SB with prior works on music restoration models. In addition to having better generation quality, our method is end-to-end without a vocoder or a codec, supports multiple restoration tasks, applies to high sampling rate, and supports restoration for very long audio. We aim to provide a detailed study of our proposed approaches for achieving these properties, and note that many of our solutions can be incorporated into prior frameworks. ♠ Liu et al. (2024) and Liu et al. (2023b); ♦ Wang et al. (2023); ♣ Moliner et al. (2023) and Moliner & Välimäki (2023).

Model	End-to-end	Multiple tasks	Sampling rate	Long audio restoration
Conditional diffusion model ♠	✗	✗	48kHz	✗
Instruction based model ♦	✗	✓	22.05kHz	✗
Inverse method ♣	✓	✓	22.05kHz	✗
A^2SB	✓	✓	44.1kHz	✓

\mathcal{X} via a forward and a backward stochastic differential equation (SDE). The forward SDE is

$$dX_t = f_t(X_t)dt + \sqrt{\beta_t}dW_t, \quad (1)$$

where $t \in [0, 1]$ is the diffusion time index such that $X_0 \sim p_{\text{data}}$ and $X_1 \sim \mathcal{N}(0, I)$, f_t is an optional drift term linear in X_t , and W_t is the Wiener process (Anderson, 1982). The reverse SDE can be analytically solved as

$$dX_t = [f_t(X_t) - \beta_t \nabla_{X_t} \log p(X_t, t)]dt + \sqrt{\beta_t}d\bar{W}_t, \quad (2)$$

where $p(X_t, t)$ is the marginal distribution of the forward SDE at time t , $\nabla_{X_t} \log p$ is its score function, and \bar{W}_t is the reverse Wiener process. Then, a neural network $\epsilon(X_t, t)$ is trained to predict the score function, making it feasible to numerically sample from the approximated data distribution.

Diffusion models can be easily extended to conditional generation by conditioning X_t on the condition y everywhere in the forward and reverse SDEs. In practice, this is done by adding y as an input to the neural network ϵ . Different conditioning mechanisms have been proposed, such as concatenation at the input (Saharia et al., 2022) or cross attention at each block (Rombach et al., 2022). While this is a flexible framework for conditional generation, the generation quality heavily depends on the empirical conditioning mechanism, and there is no explicit regularization for the output to be faithful to the condition. This casts challenges to controllable generalization especially in data restoration.

2.2 INVERSE PROBLEMS

Let \mathcal{A} be a degradation mechanism (e.g., temporal masking or bandwidth limitation) and $y = \mathcal{A}(X_0)$ be the degraded observation of the clean data X_0 . Inverse problems aim to restore X_0 from y without training a conditional model. When \mathcal{A} is affine, this becomes the linear inverse problem, and many works have proposed to modify the inference algorithm using a pre-trained unconditional model (Ho et al., 2022; Chung et al., 2022a,b; Song et al., 2023). In detail, one could estimate the score $\nabla_{X_t} \log p(y|X_t, t)$ and add it to the original score $\nabla_{X_t} \log p(X_t, t)$ similar to classifier guidance:

$$\nabla_{X_t} \log p(X_t, t|y) = \nabla_{X_t} \log p(X_t, t) + \nabla_{X_t} \log p(y|X_t, t). \quad (3)$$

The major advantage of this approach is that the same unconditional model could be applied to many restoration tasks as long as \mathcal{A} is known and affine. The output is also regularized to be faithful to y . However, the generation quality heavily depends on the quality of the unconditional model (which is more challenging to train than conditional generation) and the estimation quality of $\nabla_{X_t} \log p(y|X_t, t)$.

2.3 SCHRÖDINGER BRIDGES

Schrödinger Bridges (De Bortoli et al., 2021; Chen et al., 2021; Liu et al., 2023a; Albergo et al., 2023) are a different approach to solve inverse problems. These models generalize diffusion models to the setting where X_1 is drawn from a pre-defined $p_{\text{deg}}(X_1|X_0)$ instead of the standard normal distribution. For instance, p_{deg} can be a Gaussian distribution with mean $\mathcal{A}(X_0)$. The forward SDE is

$$dX_t = [f_t(X_t) + \beta_t \nabla_{X_t} \log \Psi(X_t, t)]dt + \sqrt{\beta_t}dW_t, \quad (4)$$

and the backward SDE is

$$dX_t = [f_t(X_t) - \beta_t \nabla_{X_t} \log \hat{\Psi}(X_t, t)]dt + \sqrt{\beta_t} d\bar{W}_t, \quad (5)$$

where $\Psi, \hat{\Psi}$ are energy potentials that solve certain coupled PDEs (Schrödinger, 1932; Léonard, 2013). In Liu et al. (2023a), the drift term is defined as $f_t = 0$, leading to an analytic solution to the posterior distribution $q(X_t|X_0, X_1) = \mathcal{N}(X_t; \mu_t, \Sigma_t)$ under the Dirac delta assumption (see (9)). Then, a neural network $\epsilon(X_t, t)$ is trained to predict $(X_t - X_0)$ up to a scaling factor. Sampling from the reverse SDE is similar to the diffusion models, except that one starts from a given X_1 instead of the random noise. Schrödinger Bridges embody the advantages of both conditional diffusion models and inverse algorithms: (1) the generation quality is similar to conditional diffusion model as it is trained on paired data, and (2) the generation is faithful to X_1 as the reverse SDE starts with X_1 . These make Schrödinger Bridges suitable for data restoration, especially when X_1 is in part aligned with X_0 . Therefore, we leverage the Schrödinger Bridge framework for audio restoration.

2.4 AUDIO RESTORATION

Audio restoration problems are inverse problems in the audio domain, where the degradation function is audio-specific including but not limited to low-pass filtering (or down-sampling), masking temporal segments, adding noise, and so on (see Table 3 in Serrà et al. (2022) for a more comprehensive summary of degradations). The corresponding tasks for these corruptions are called bandwidth extension (up-sampling), inpainting, denoising, etc. Our work focuses on music bandwidth extension and inpainting at 44.1kHz, as these are more challenging tasks than speech restoration tasks, which are often tackled at 16kHz.

Many diffusion-based approaches have been proposed for audio restoration. Most existing works are designed for speech restoration, where they use conditional diffusion models to restore degraded magnitude, and then apply a vocoder to produce the waveform (Serrà et al., 2022; Yu et al., 2023; Moliner & Välimäki, 2023; Kim et al., 2024; Yun et al., 2025). There are a few models for music restoration: NuWave (Lee & Han, 2021) and AudioSR (Liu et al., 2024) for bandwidth extension, and MAID (Liu et al., 2023b) for inpainting. Moreover, with the recent success of multimodal models, instruction-based models have been proposed for audio restoration (Wang et al., 2023), where the specific restoration task can be defined by text instructions.

Several other works are based on the inverse problem framework. CQT-Diff (Moliner et al., 2023) is a linear inverse problem approach for audio restoration. It trains an end-to-end 22.05kHz unconditional model with constant-Q transform (CQT) instead of short-term Fourier transform (STFT), and then applies the inverse algorithms proposed by Ho et al. (2022) for restoration. Moliner & Välimäki (2023) improved their architecture and applied to inpainting with a gap of up to 300 ms. We refer to Lemercier et al. (2024) for a comprehensive survey of diffusion models for audio restoration. There are also several orthogonal works using Schrödinger Bridges for speech enhancement (Jukić et al., 2024; Wang et al., 2024; Li et al., 2025).

Our work targets at the challenging music bandwidth extension and inpainting tasks at 44.1kHz. We use Schrödinger Bridges and achieve significantly better restoration quality. Our model is end-to-end requiring no vocoder, supports these restoration tasks with a single model, applies to high sampling rate, and can restore very long audio. Table 1 summarizes the comparison between our approach and existing works in the music restoration domain.

3 METHOD

Our *A²SB* is an end-to-end approach for music restoration at 44.1kHz that does not require a pre-trained vocoder or audio codec. We achieve this by training on an effective factorized audio representation (see Section 3.1). We then train a Schrödinger Bridge model for music restoration based on Liu et al. (2023a), with specific alterations for handling our audio representation (see Section 3.2). Since phase predictions are free-form and may not be proper, Section 3.3 describes how we obtain waveform with the model outputs. Section 3.4 describes our network architecture. Section 3.5 describes our two-stage training paradigm. Section 3.6 describes an inference algorithm that supports arbitrarily long audio inputs without boundary artifacts.

For notations, we let $\tilde{X} \in [-1, 1]^L$ be the 1-D raw waveform of clean audio with length L , and X_t be the audio representation that we will use in the Schrödinger Bridge model at time t with respect to the stochastic process. We ignore the subscript t when there is no ambiguity.

3.1 MAGNITUDE-PHASE FACTORIZED AUDIO REPRESENTATION

The short-time Fourier transformation (STFT) representation of \tilde{X} , $S = \text{STFT}(\tilde{X})$, is a complex matrix in $\mathbb{C}^{N \times W}$, where N is the number of frequency subbands and W is the number of overlapping STFT frames.¹ For simplicity, we can represent the complex values with their real and imaginary parts $[\text{Re}(S), \text{Im}(S)]$, leading to the two-channel spectrogram $S \in \mathbb{R}^{N \times W \times 2}$. While existing vocoder-free methods directly model this two-channel representation (Richter et al., 2023; Jukić et al., 2024; Wu et al., 2024), we factorize S into magnitude and phase components of the STFT in our method. We find that separating them is necessary for the following reasons:

1. Magnitudes in adjacent frequency bands are strongly correlated, but this is less true for phase. Keeping them entangled would make it harder for the model to capture smooth changes in magnitude across frequencies.
2. The periodicity of phase makes fitting to it a more challenging task. In addition, phase estimation involves computing the ratio of the real and imaginary components, both of which would be near-zero floating point values at low magnitudes.
3. Phase-magnitude factorization limits the extent to which complications from fitting to the phase affect the magnitude estimation.

To factorize S into magnitude Λ and phase Θ we compute:

$$\begin{cases} \Lambda_{i,j} &:= \sqrt{(S_{i,j,1})^2 + (S_{i,j,2})^2} \\ \Theta_{i,j} &:= \text{atan2}(S_{i,j,2}, S_{i,j,1}) \end{cases} . \quad (6)$$

We further use the trigonometric representation to model the phase Θ (Peer & Gerkmann, 2022). The trigonometric projections can be interpreted as the original two-channel spectrogram S with normalized magnitude (i.e., all magnitudes = 1). Our final factorized representation $X \in \mathbb{R}^{N \times W \times 3}$ is defined as:

$$\begin{cases} X_{i,j,1} &:= (\Lambda_{i,j})^\rho \\ X_{i,j,2} &:= \cos(\Theta_{i,j}) \\ X_{i,j,3} &:= \sin(\Theta_{i,j}) \end{cases} . \quad (7)$$

We set $\rho < 1$ to compress the range of the magnitude values, using $\rho := 0.25$ in our experiments. Our experiments in 4.5 find that the factorized representation results in a better fit to the data distribution than the un-factorized S .

3.2 MUSIC RESTORATION WITH SCHRÖDINGER BRIDGES

We train a Schrödinger Bridge model on the three-channel representation X described in (7). Following Liu et al. (2023a), we let $X_0 \in \mathbb{R}^{N \times W \times 3}$ be the clean sample inputs, and X_1 be degraded samples. We focus on bandwidth extension and inpainting, both of which can be formulated as the masking corruption similar to image inpainting. Let $\mathbb{M} \in \mathbb{B}^{N \times W \times 3}$ be the boolean mask for masking, where $\mathbb{B} = \{0, 1\}$. For bandwidth extension, $\mathbb{M}_{i,j,k} = 1$ for $i > N'$, where N' refers to the highest subband in the degraded audio. N' is randomly sampled from subbands representing frequencies above 4kHz. For inpainting, $\mathbb{M}_{i,j,k} = 1$ for $W_1 \leq j \leq W_2$, where W_1 and W_2 refer to the starting and ending frame of missing audio. Following Liu et al. (2023b), we randomly sample W_1 and W_2 such that the inpainting gap is uniform between 0.1 and 1.6 seconds. For a certain mask \mathbb{M} , we define X_1 as

$$X_1 = X_0 \odot (1 - \mathbb{M}) + \eta_{\text{fill}} \odot \mathbb{M}, \quad (8)$$

where \odot refers to the element-wise product, and $\eta_{\text{fill}} \sim \mathcal{N}(0, \sigma_{\text{fill}}^2 I)$ in order to define a Gaussian $p_{\text{deg}}(X_1 | X_0)$ for the masked area in our audio representation. Note that if $\mathbb{M} = 1$ and $\sigma_{\text{fill}} = 1$, the Schrödinger Bridge degenerates to an unconditional diffusion model, where X_1 is Standard Normal.

¹We assume a 44.1kHz sampling rate, with hop size = 512, window length = 2048, and FFT bins = 2048. We train with $W = 256$, which corresponds to about 2.97 seconds of audio.

According to Liu et al. (2023a), X_t is sampled from $q(X_t|X_0, X_1) = \mathcal{N}(X_t; \mu_t, \Sigma_t)$, where μ_t and Σ_t equal to

$$\mu_t = \frac{\bar{\sigma}_t^2 X_0 + \sigma_t^2 X_1}{\bar{\sigma}_t^2 + \sigma_t^2}, \Sigma_t = \frac{\bar{\sigma}_t^2 \sigma_t^2 I}{\bar{\sigma}_t^2 + \sigma_t^2}, \quad (9)$$

where $\sigma_t^2 = \int_0^t \beta_\tau d\tau$, $\bar{\sigma}_t^2 = \int_t^1 \beta_\tau d\tau$. The β_t schedule is symmetric on each side of $t = \frac{1}{2}$: $\beta_t = \beta_{1-t} = \min(t, 1-t)^2 \cdot \beta_{\max}$, where β_{\max} is a hyper-parameter to tune. In our model, we use $\beta_{\max} = 1$ as it leads to the most stable training. The training objective is only computed on masked region of our audio representation:

$$\mathcal{L}(\epsilon) = \mathbb{E}_{t \sim \mathcal{U}([0,1]), \mathbb{M}, X_0 \sim \mathcal{X}, X_t \sim q(X_t|X_0, X_1)} \left\| \mathbb{M} \odot \left(\epsilon(X_t, t) - \frac{X_t - X_0}{\sigma_t} \right) \right\|_2^2, \quad (10)$$

where t is sampled from the uniform distribution on $[0, 1]$, X_0 is sampled from \mathcal{X} , X_t is sampled from $q(X_t|X_0, X_1)$, ϵ is the neural network taking both X_t and step t as inputs, and \mathbb{M} is uniformly sampled from the bandwidth extension and inpainting masks.

3.3 WAVEFORM SYNTHESIS WITH PHASE ORTHOGONALIZATION

All operations defined in Section 3.1 are invertible and should allow us to recover the original 1-D waveform signal almost exactly. We can reconstruct the two-channel spectrogram \hat{S} from X with:

$$\begin{cases} \hat{S}_{i,j,1} = X_{i,j,2} \cdot (X_{i,j,1})^{1/\rho} \\ \hat{S}_{i,j,2} = X_{i,j,3} \cdot (X_{i,j,1})^{1/\rho} \end{cases}. \quad (11)$$

Then, applying the inverse STFT with the same STFT parameters yields the waveform.

However, when sampling from our trained neural network, we cannot guarantee that the unconstrained model outputs $[X_{i,j,2}, X_{i,j,3}]$ satisfy the trigonometric representation of phase: $X_{i,j,2}^2 + X_{i,j,3}^2 = 1$. This could manifest as an additional scaling of the reconstructed spectrogram S , which is undesirable. To alleviate this issue, we use phase orthogonalization to map $[X_{i,j,2}, X_{i,j,3}]$ to the last-squares-nearest valid configuration. This is in part inspired by the analysis in Levinson et al. (2020) for learning 3D rotations, though we require only the 2D rotations in our case. Furthermore, the least-squares optimality of SVD orthogonalization is ideal for the removal of small amounts of Gaussian noise, making it compatible with the Gaussian diffusion process. Approaches such as Chen & Lipman (2023) can also guarantee proper rotation values, but we find our approach to be simple and practical enough for our use case.

Let $\hat{R}_{i,j} \in \mathbb{R}^{2 \times 2}$ be a noisy estimate of a rotation matrix at spectrogram coordinate (i, j) , which is constructed with

$$\hat{R}_{i,j} := \begin{bmatrix} X_{i,j,2} & -X_{i,j,3} \\ X_{i,j,3} & X_{i,j,2} \end{bmatrix}. \quad (12)$$

We then compute its nearest valid configuration in least squares as follows:

$$\text{SVD}^+(\hat{R}_{i,j}) := \underset{R_{i,j} \in \text{SO}(2)}{\operatorname{argmin}} \|R_{i,j} - \hat{R}_{i,j}\|_F^2, \quad (13)$$

where $\text{SO}(2)$ is the orthogonal group in two dimensions. Note that for any 2×2 matrix A , we have the following solution (Levinson et al., 2020; Schönemann, 1966):

$$\text{SVD}^+(A) = U \Sigma' V, \text{ where } \Sigma' = \text{diag}(1, \det(UV^\top)), \quad (14)$$

where $A = U \Sigma V$ is the SVD decomposition. Applying SVD to $\hat{R}_{i,j}$ yields

$$U = (X_{i,j,2}^2 + X_{i,j,3}^2)^{-\frac{1}{2}} \hat{R}_{i,j}, \Sigma = (X_{i,j,2}^2 + X_{i,j,3}^2)^{\frac{1}{2}} I, V = I. \quad (15)$$

And therefore, the solution is

$$\text{SVD}^+(\hat{R}_{i,j}) = (X_{i,j,2}^2 + X_{i,j,3}^2)^{-\frac{1}{2}} \hat{R}_{i,j} \quad (16)$$

as $\det(UV^\top) = 1$. Then, the orthogonalized phase estimation allows us to reconstruct the spectrogram with

$$\hat{S}_{i,j} = (X_{i,j,1})^{1/\rho} \cdot (\text{SVDO}^+(\hat{R}_{i,j}))_{:,1}. \quad (17)$$

We further compute the minimum residual as

$$\text{Err}_{\text{phase-ortho}}(X_{i,j}) = \|\text{SVDO}^+(\hat{R}_{i,j}) - \hat{R}_{i,j}\|_F^2 = 2 \left((X_{i,j,2}^2 + X_{i,j,3}^2)^{\frac{1}{2}} - 1 \right)^2. \quad (18)$$

We will quantify and visualize this error in our experiments. We expect a well trained model should have a small error, and the phase orthogonalization only does minor correction.²

3.4 ARCHITECTURE

Our model closely follows the conditional UNet architecture as commonly used in prior works (Ronneberger et al., 2015; Dhariwal & Nichol, 2021; Liu et al., 2023a), with some modifications. Notably, absolute positional embedding layers were replaced with 2-D rotary position embedding (RoPE) (Su et al., 2024). Further, we use an additional conditioning variable $C \in \mathbb{R}^{N \times W}$ via absolute positional embeddings. C only varies in the frequency axis: $C_{i,j} = i$, $1 \leq i \leq N$. This allows the model to strongly condition on the frequency, while maintaining translational equivariance along the temporal axis in the spectrogram.

In terms of the neural network configuration, there are five up-sampling and down-sampling layers, each having two residual blocks. The hidden channels are [128, 256, 512, 768, 1024, 2048]. Both input and output have three channels, following our audio representation in (7). The diffusion step embedding dimension is 128, following Kong et al. (2021). The network has 565M parameters.

3.5 TWO-STAGE TRAINING

We follow the common pre-training and fine-tuning approach for stable large scale training (Ouyang et al., 2022). During pre-training, we train our Schrödinger Bridge model from scratch on 2.3K hours of training data. We use `bf16` for more efficient training. During fine-tuning, we train on a 1.5K-hour high quality subset and use `fp32`, ensuring the model produces clean and meaningful sound for corrupted parts.

During pre-training, we use as much data as possible to train our model from scratch. We use `bf16` for more efficient training. During fine-tuning, we only train on high quality subsets of the data with `fp32`, ensuring the model produces clean and meaningful sound for corrupted parts. In detail, the fine-tuning set includes: FMA (Defferrard et al., 2016), Medley-solos-DB (Lostanlen & Cella, 2016), MTG-Jamendo (Bogdanov et al., 2019), Musan (Snyder et al., 2015), Music Instrument (Mutlu, 2024), MusicNet (Thickstun et al., 2017), and Slakh (Manilow et al., 2019). The pre-training set additionally includes: CLAP-Freesound (Wu et al., 2023), GTZAN (Sturm, 2013), MusicCaps (Agostinelli et al., 2023), NSynth (Engel et al., 2017), PianoTriads (Roberts, 2022). We carefully examined all data licenses in these datasets and only selected the permissively licensed audio to train our model (i.e., we removed data that are NC, ND, SA, or under unknown licenses, etc.).

During fine-tuning, we adopt the t -range partitioning strategy from Balaji et al. (2022): we fine-tune separate models on different t intervals, each initialized from the same pre-trained checkpoint. This leads to models specialized in different noise level ranges. We choose the intervals that partition noise level ranges between σ_0^2 and σ_1^2 . In 2-partitioning, the intervals are $t \in (0, \frac{1}{2}]$ and $t \in [\frac{1}{2}, 1]$; in 4-partitioning, the intervals are $t \in (0, \frac{1}{2^{4/3}}]$, $t \in [\frac{1}{2^{4/3}}, \frac{1}{2}]$, $t \in [\frac{1}{2}, 1 - \frac{1}{2^{4/3}}]$, and $t \in [1 - \frac{1}{2^{4/3}}, 1]$. During sampling, we use the corresponding checkpoint based on the exact t .

3.6 SAMPLING

The sampling algorithm given X_1 directly follows the diffusion model (Ho et al., 2020). Let Δt be a step size where $\frac{1}{\Delta t}$ is an integer referring to the number of sampling steps. There is an analytic form

²We additionally note that manifold generative models such as Chen & Lipman (2023) could also address this issue without orthogonalization, yet we find our approach simple and effective enough and therefore leave this approach for future work.

Algorithm 1 MultiDiffusion sampling at step t

```

Input:  $\mathbf{X}_t^{\text{full}} \in \mathbb{R}^{N \times W^{\text{full}} \times 3}$ ,  $t$ ,  $W$ ,  $H$ ,  $\epsilon(\cdot, \cdot)$ 
/* Input noisy spectrogram tensor, sampling timestep, window size, MultiDiffusion
   hop size, model. Tensors are in bold. */
1  $\mathbf{C}, \mathbf{V} \leftarrow \mathbf{0} \in \mathbb{R}^{N \times W^{\text{full}} \times 3}$  /* Initialize normalizing & output tensor. */
2  $j \leftarrow 0$  /* window left-most position index (numpy-style indexing) */
3 while  $j + W < W^{\text{full}}$  do
4    $\mathbf{X}_t^{\text{patch}} \leftarrow \mathbf{X}_t^{\text{full}}[:, j : (j + W), :]$  /* Create a patch. */
   /* Accumulate model output and normalizing tensors. */
5    $\mathbf{V}[:, j : (j + W), :] \leftarrow \mathbf{V}[:, j : (j + W), :] + \epsilon(\mathbf{X}_t^{\text{patch}}, t)$ 
6    $\mathbf{C}[:, j : (j + W), :] \leftarrow \mathbf{C}[:, j : (j + W), :] + 1$ 
7    $j \leftarrow j + H$  /* Shift processing window by hop size. */
8 return  $\mathbf{V} \oslash \mathbf{C}$  /* Average with element-wise division. */

```

for the posterior (see proof of Proposition 3.3 in Liu et al. (2023a)):

$$p(X_{t-\Delta t} | X_0, X_t) = \mathcal{N} \left(\frac{(\Delta \sigma_t^2) X_0 + \sigma_t^2 X_t}{\Delta \sigma_t^2 + \sigma_t^2}, \frac{(\Delta \sigma_t^2) \sigma_t^2}{\Delta \sigma_t^2 + \sigma_t^2} I \right), \quad (19)$$

where $\Delta \sigma_t^2 := \sigma_t^2 - \sigma_{t-\Delta t}^2$. During sampling, the X_0 is replaced with the predicted $X_0 := X_t - \sigma_t \epsilon(X_t, t)$ as indicated by (10). Then, repeating (19) for $\frac{1}{\Delta t}$ steps yields the final output.

In practice, the audio we would like to up-sample or inpaint may be much longer than our training segment length. This is similar to the panorama generation problem in image generation, which could be solved by MultiDiffusion (Bar-Tal et al., 2023). Inspired by their approach, we apply MultiDiffusion to extend our sampling process to arbitrary length. Our algorithm is similar to Algorithm 2 in Bar-Tal et al. (2023), where the condition is the degraded audio in our case.

Formally, let $X_t^{\text{full}} \in \mathbb{R}^{N \times W^{\text{full}} \times 3}$ be a degraded sample of arbitrary length that we would like to up-sample or inpaint. For simplicity, we assume $W^{\text{full}} = KW$ where $K > 1$. ³ Our trained model $\epsilon(\cdot, t)$ can process inputs of size $N \times W \times 3$ where W corresponds to 256 STFT frames (2.97 seconds). At diffusion time t , we compute the model's output on the full sample $\epsilon(X_t^{\text{full}}, t)$ as follows. We process our input X_t^{full} with a sliding window of width W and shifting the position by a hop size $H < W$ (typically 128 for 50% overlap) until all of X_t is processed. Outputs in overlapping areas are uniformly averaged, though other weighting functions are topic of future work (Polyak et al., 2024). Cyclic padding is used to ensure the last input window has a full temporal width of W . Our MultiDiffusion processing is detailed in (20) and the pseudo code is in Algorithm 1.

$$\begin{aligned}
\mathbf{int}_k &= \left[\frac{k-1}{2}W : \frac{k+1}{2}W \right], k = 1, \dots, 2K-1; \\
\mathbf{v}_k &= \epsilon(\mathbf{crop}(X_t^{\text{full}}, \mathbf{int}_k), t), k = 1, \dots, 2K-1; \\
\epsilon(X_t^{\text{full}}, t) &:= \left(\sum_{k=1}^{2K-1} \mathbf{pad}(\mathbf{v}_k, \mathbf{int}_k) \right) \oslash \left(\sum_{k=1}^{2K-1} \mathbf{pad}(\mathbf{1}_{N \times W \times 3}, \mathbf{int}_k) \right),
\end{aligned} \quad (20)$$

where

- \mathbf{int}_k refers to the k -th interval in the sliding-window segmentation of the full sample with $W/2$ overlapping frames between consecutive segments,
- \mathbf{crop} refers to the cropping operation applied to the full sample given the interval indicating start and end frames,
- \mathbf{pad} refers to the zero-padding (to shape of full sample) operation applied to a segment given the interval indicating start and end frames in the full sample (note that \mathbf{pad} is a right inverse function of \mathbf{crop}),
- and \oslash is the element-wise division symbol (inverse function of \odot).

³The arbitrary length case can be easily tackled with padding in the end.

4 EXPERIMENTS

4.1 EXPERIMENTAL SETUP

A²SB. We train different configurations of our model as described in Section 3.5: no partitioning, 2-partitioning, and 4-partitioning.⁴ For all of our models, we pre-train with a batch size of 320 for 209K iterations, and fine-tune with a batch size of 64 for additional 250K iterations. We use gradient clip = 0.5 and learning rate 8×10^{-5} . The training segment length is 130560, which equals about 2.97 seconds of audio. We sample the area removal mask in (8) uniformly from the inpainting mask and the bandwidth extension mask. We use 32 NVIDIA A100 GPUs to train our models. At inference time, we use 50 sampling steps for bandwidth extension, and 200 sampling steps for inpainting.

Baselines. For each of the bandwidth extension and inpainting task, we consider three baselines: conditional diffusion method, inverse method, and instruction-based method.

- **Conditional diffusion.** We use *AudioSR* (Liu et al., 2024) for bandwidth extension. *AudioSR* could extend audio to 48kHz with training segment length 5.12 seconds. We consider *MAID* (Liu et al., 2023b) for inpainting. *MAID* could inpaint audio at 44.032kHz with training segment length 131072. We re-train *MAID* on our training dataset.
- **Inverse method.** We consider *CQTDiff* (Moliner et al., 2023) for both tasks. Since the original *CQTDiff* is small and trained on 22.05kHz, we re-train a larger *CQTDiff* on 44.1kHz using our training dataset. We increase the depth from 6 to 8 and double the channels to [64, 128, 128, 256, 256, 256, 256, 256], leading to a $5.75 \times$ larger model. It is the largest model we find to have stable training in our experiments.
- **Instruction-based method.** Since existing instruction-based models (Wang et al., 2023) are only 24kHz or less, we train our own 48kHz instruction-based baseline model on our training dataset with the following design. We use the instruction templates for up-sampling and inpainting from *Audit* (Wang et al., 2023), an optimized diffusion transformer architecture (Peebles & Xie, 2023) similar to Lee et al. (2024), the byT5 embedding (Xue et al., 2022), the optimal-transport conditional flow matching loss function (Lipman et al., 2022; Tong et al., 2023), and a 48kHz BigVGAN-v2 vocoder (Lee et al., 2023). For conciseness, we name this model *IBAR*: Instruction-Based Audio Restoration.

Evaluation setup. We evaluate all models on several 44.1kHz out-of-distribution (OOD) test sets:

- AAM (Ostermann et al., 2023): a collection of synthetic music. We randomly select 93 test samples for evaluation. Each sample is between 2 and 3 minutes.
- CCMixter⁵: a collection of remixed music. We use the same set as Liutkus et al. (2014). Each sample is between 1 and 6 minutes.
- MTD (Zalkow et al., 2020): a collection of classical music pieces. We randomly select 200 test samples for evaluation. Each sample is between 10 seconds and 1 minute.

Our bandwidth extension evaluation follows Liu et al. (2024) and evaluates three cutoff frequencies: 4kHz, 8kHz, and 12kHz. We resample the ground truth audio to twice the cutoff frequency and use it as the input to all models. For the inpainting evaluation, we mask a fixed-length (300ms, 500ms, 1000ms) segment every 5 seconds. We then run the model with its receptive field centered on each masked region to inpaint the missing content.

For **objective evaluation metrics**, we report the following.

- Log-spectral distance (LSD) (Erell & Weintraub, 1990), a spectrogram distance metric computed as

$$LSD = \frac{1}{W} \sum_{j=1}^W \left[\frac{1}{N} \sum_{i=1}^N \left(\log_{10} \frac{\Lambda_{i,j}^2}{\hat{\Lambda}_{i,j}^2} \right)^2 \right]^{\frac{1}{2}}, \quad (21)$$

⁴For the 4-partitioning model, we apply an additional loss mask to compute loss only up to the maximum frequency of each training segment to make training more stable.

⁵<https://ccmixter.org/>

where Λ is the ground truth magnitude and $\hat{\Lambda}$ the magnitude of the model’s prediction.

- Scale-invariant spectrogram-to-noise ratio (SiSpec) (Liu et al., 2021), a signal-to-noise ratio metric computed as

$$\text{SiSpec} = 10 \cdot \log_{10} \frac{\|\mathbf{n}(\Lambda)\|^2}{\|\mathbf{n}(\Lambda) - \hat{\Lambda}\|^2}, \quad (22)$$

where $\mathbf{n}(\Lambda) = \langle \hat{\Lambda}, \Lambda \rangle \Lambda / \|\hat{\Lambda}\|^2$ is the scale invariant normalization of the ground truth magnitude.

- ViSQOL (Chinen et al., 2020), an objective perceptual quality for 48kHz audio, which measures similarity scores by comparing the spectro-temporal features and maps to the Mean Opinion Score (MOS) scale between 1 and 5. The ground truth has a score of 4.732.

In addition to the above evaluation datasets, we train and evaluate all models on the Maestro dataset (Hawthorne et al., 2019), a dataset of classic piano music. In addition to LSD and SiSpec, we compute the F₁ score of MIDI transcriptions using the `mir_eval` package (Raffel et al.).

We conduct **human evaluation** on the bandwidth extension (cutoff = 4kHz) and inpainting (gap = 1000ms) experiments due to the limitations of objective metrics. For each OOD test dataset, we randomly select fifty segments and ask human listeners to rate the output quality based on how close they sound compared to the ground truth and report Mean Opinion Scores (MOS).

4.2 BANDWIDTH EXTENSION RESULTS

The bandwidth extension results are shown in Tables 2 - 5. We find our *A²SB* achieves better SiSpec in most cases, indicating it has the best signal-to-noise ratio (SNR) and therefore the least noise up to a scale transformation. *A²SB* also achieves consistently better ViSQOL, indicating the samples have perceptually better quality. Our instruction based audio restoration baseline (IBAR) achieves better LSD in most cases, indicating it models the absolute value of the magnitude most accurately. Nevertheless, *A²SB* still achieves very good LSD compared to other baselines, and especially achieves similar LSD as IBAR on AAM, without using a vocoder.

Comparing different t -range partitioning approaches in *A²SB*, we find the 2-partitioned model (on $t \in (0, \frac{1}{2}]$ and $t \in [\frac{1}{2}, 1]$) yields the better results overall. We conclude that two models trained on each splitted t -range are more expert than the model trained on $t \in (0, 1]$ without partitioning. We also find that having more partitions helps modeling classic music (MTD) especially on the perceptual quality, and therefore we report the 4-partitioning results on Maestro.

In Figure 2, we show a qualitative sample of different bandwidth extension baselines. More samples can be found in Appendix A. AudioSR often has artifacts around the cutoff frequency (Figures 14 and 15), and it sometimes hallucinates on high frequency regions by adding percussion sounds (Figure 13). CQTDiff usually has much worse quality. IBAR sometimes has unsMOOTH generations across frames, and it occasionally fails to produce a meaningful output. *A²SB* generates better quality overall, produces smoother and consistent content, and keeps the beats stable without hallucination on beats and percussion.

Table 2: Bandwidth extension results on AAM (synthetic music).

Method	Cutoff = 4kHz			Cutoff = 8kHz			Cutoff = 12kHz		
	LSD ↓	SiSpec ↑	ViSQOL ↑	LSD ↓	SiSpec ↑	ViSQOL ↑	LSD ↓	SiSpec ↑	ViSQOL ↑
AudioSR	2.22	13.73	3.057	1.94	14.61	3.455	1.62	19.93	3.783
CQTDiff	2.37	19.91	1.926	2.39	22.22	1.928	2.42	22.63	1.965
IBAR	1.38	8.51	2.951	1.16	10.82	3.384	0.99	12.31	4.102
<i>A²SB</i> (no partitioning)	1.40	19.28	3.004	1.15	27.35	3.412	0.99	31.33	3.947
<i>A²SB</i> (2-partitioning)	1.44	23.03	3.248	1.15	28.69	3.706	0.99	31.76	4.231
<i>A²SB</i> (4-partitioning)	1.49	22.59	3.110	1.20	28.46	3.773	1.04	31.67	4.340

Table 3: Bandwidth extension results on CCMixer (remixed music).

Method	Cutoff = 4kHz			Cutoff = 8kHz			Cutoff = 12kHz		
	LSD ↓	SiSpec ↑	ViSQOL ↑	LSD ↓	SiSpec ↑	ViSQOL ↑	LSD ↓	SiSpec ↑	ViSQOL ↑
AudioSR	2.00	12.50	2.746	1.86	14.93	3.097	1.75	18.35	3.510
CQTDiff	2.01	14.67	1.970	2.06	15.88	1.860	2.10	16.34	1.850
IBAR	1.64	7.11	2.373	1.41	10.46	2.604	1.36	7.86	2.744
A^2SB (no partitioning)	1.93	14.05	2.770	1.71	19.95	3.200	1.48	27.17	4.047
A^2SB (2-partitioning)	1.85	18.00	2.851	1.62	23.39	3.438	1.45	29.26	4.211
A^2SB (4-partitioning)	1.84	17.46	2.657	1.65	23.17	3.430	1.50	29.20	4.234

Table 4: Bandwidth extension results on MTD (classical music).

Method	Cutoff = 4kHz			Cutoff = 8kHz			Cutoff = 12kHz		
	LSD ↓	SiSpec ↑	ViSQOL ↑	LSD ↓	SiSpec ↑	ViSQOL ↑	LSD ↓	SiSpec ↑	ViSQOL ↑
AudioSR	1.75	21.74	3.391	1.81	27.26	3.226	1.85	28.97	3.150
CQTDiff	1.74	10.62	1.747	1.63	17.42	1.777	1.57	21.62	2.000
IBAR	1.12	12.31	2.995	0.92	12.94	3.525	0.85	13.08	3.843
A^2SB (no partitioning)	1.33	25.51	2.557	1.05	33.10	3.201	0.87	35.34	3.936
A^2SB (2-partitioning)	1.29	28.15	3.101	1.07	34.36	3.718	0.88	35.97	4.200
A^2SB (4-partitioning)	1.77	27.56	3.446	1.59	34.25	3.829	1.51	36.07	4.274

Table 5: Bandwidth extension results on Maestro (classical piano music with MIDI).

Method	Cutoff = 4kHz			Cutoff = 8kHz			Cutoff = 12kHz		
	LSD ↓	SiSpec ↑	F ₁ ↑	LSD ↓	SiSpec ↑	F ₁ ↑	LSD ↓	SiSpec ↑	F ₁ ↑
CQTDiff	1.154	31.49	0.761	1.137	32.99	0.772	1.129	33.33	0.774
IBAR	0.769	12.69	0.769	0.688	12.22	0.757	0.616	13.48	0.770
A^2SB (4-partitioning)	0.773	34.32	0.910	0.659	41.69	0.910	0.545	42.60	0.910

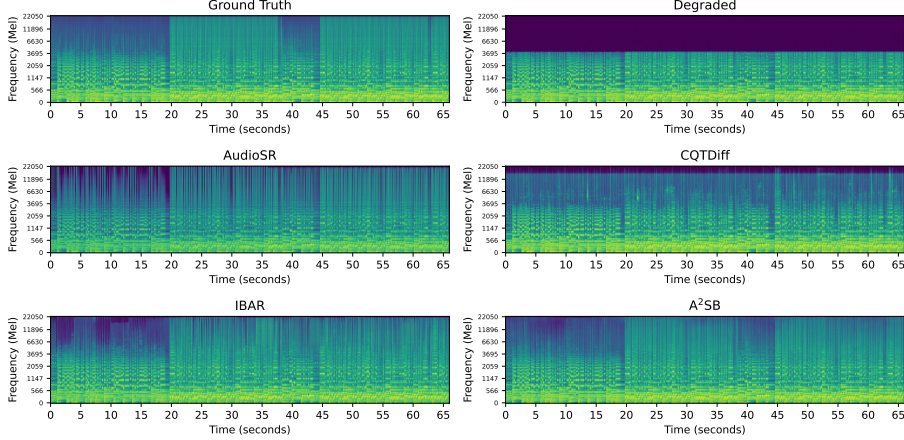


Figure 2: Qualitative comparison between different bandwidth extension methods with cutoff = 4kHz.

4.3 INPAINTING RESULTS

The inpainting results are shown in Tables 6 - 9. A^2SB achieves consistently better evaluation results. This is likely because inpainting has a smaller synthesized-content versus context ratio than bandwidth extension. All three A^2SB models achieve similar generation quality. Models with t -range partitioning have slightly better quality than the one without partitioning, and having 4 partitions is slightly better than 2.

In Figure 3, we show a qualitative sample of different inpainting baselines. More samples can be found in Appendix B. MAID and CQTDiff have much worse quality, and A^2SB has more consistent outputs compared to that of baselines.

Table 6: Inpainting results on AAM (synthetic music).

Method	Gap = 300ms			Gap = 500ms			Gap = 1000ms		
	LSD ↓	SiSpec ↑	ViSQOL ↑	LSD ↓	SiSpec ↑	ViSQOL ↑	LSD ↓	SiSpec ↑	ViSQOL ↑
MAID	0.139	14.37	4.570	0.208	11.42	4.504	0.378	7.74	4.305
CQTDiff	1.516	14.37	4.502	1.510	11.13	4.457	1.494	7.17	4.219
IBAR	0.512	8.67	4.231	0.420	9.66	4.383	0.525	6.88	4.204
A^2SB (no partitioning)	0.081	17.10	4.660	0.128	12.72	4.592	0.257	7.90	4.432
A^2SB (2-partitioning)	0.077	17.89	4.666	0.122	13.95	4.601	0.238	9.31	4.442
A^2SB (4-partitioning)	0.076	18.36	4.673	0.121	13.96	4.613	0.238	9.16	4.465

Table 7: Inpainting results on CCMixer (remixed music).

Method	Gap = 300ms			Gap = 500ms			Gap = 1000ms		
	LSD ↓	SiSpec ↑	ViSQOL ↑	LSD ↓	SiSpec ↑	ViSQOL ↑	LSD ↓	SiSpec ↑	ViSQOL ↑
MAID	0.129	13.34	4.556	0.205	10.67	4.462	0.394	7.11	4.235
CQTDiff	1.305	11.16	4.486	1.293	9.01	4.403	1.266	5.95	4.126
IBAR	0.384	10.89	4.466	0.415	9.36	4.378	0.504	6.56	4.186
A^2SB (no partitioning)	0.088	13.83	4.625	0.139	10.68	4.537	0.274	6.61	4.336
A^2SB (2-partitioning)	0.086	15.21	4.630	0.134	12.31	4.547	0.259	8.48	4.352
A^2SB (4-partitioning)	0.086	14.89	4.632	0.135	11.88	4.549	0.261	7.96	4.358

Table 8: Inpainting results on MTD (classical music).

Method	Gap = 300ms			Gap = 500ms			Gap = 1000ms		
	LSD ↓	SiSpec ↑	ViSQOL ↑	LSD ↓	SiSpec ↑	ViSQOL ↑	LSD ↓	SiSpec ↑	ViSQOL ↑
MAID	0.139	9.86	4.406	0.223	7.29	4.285	0.430	3.79	4.044
CQTDiff	0.846	8.84	4.411	0.855	5.82	4.252	0.877	1.26	3.963
IBAR	0.293	13.62	4.136	0.306	11.71	4.109	0.346	7.93	4.030
A^2SB (no partitioning)	0.073	17.83	4.641	0.106	13.87	4.562	0.201	7.80	4.347
A^2SB (2-partitioning)	0.071	18.28	4.650	0.103	14.74	4.572	0.187	9.94	4.376
A^2SB (4-partitioning)	0.071	18.43	4.655	0.103	14.73	4.584	0.187	9.40	4.402

Table 9: Inpainting results on Maestro (classical piano music with MIDI).

Method	Gap = 300ms			Gap = 500ms			Gap = 1000ms		
	LSD ↓	SiSpec ↑	F ₁ ↑	LSD ↓	SiSpec ↑	F ₁ ↑	LSD ↓	SiSpec ↑	F ₁ ↑
MAID	0.700	8.40	0.673	0.831	6.16	0.666	1.156	2.90	0.655
CQTDiff	0.691	12.24	0.818	0.703	8.53	0.814	0.741	4.38	0.798
IBAR	0.344	12.73	0.803	0.381	9.50	0.795	0.413	6.28	0.786
A^2SB (4-partitioning)	0.134	17.03	0.870	0.167	13.33	0.854	0.254	8.45	0.820

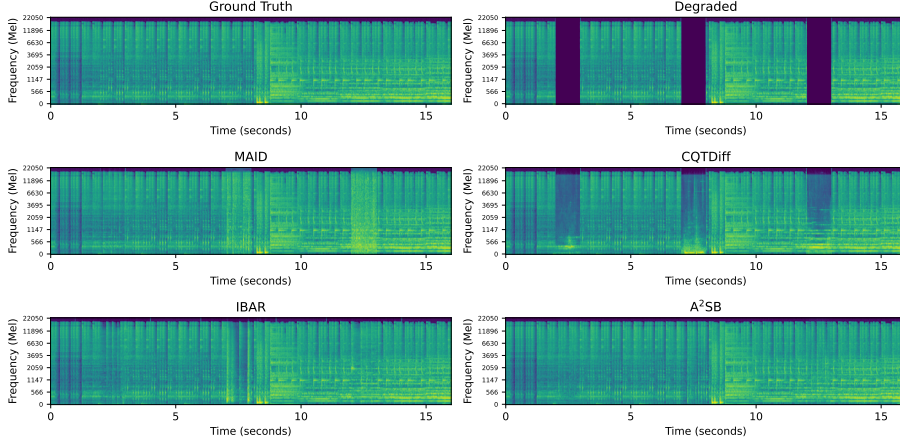


Figure 3: Qualitative comparison between different inpainting methods with inpainting gap = 1 sec.

4.4 HUMAN EVALUATION

We additionally conduct human evaluation on the bandwidth extension (cutoff = 4kHz) and inpainting (gap = 1000ms) experiments. For each OOD test dataset, we randomly select fifty segments and ask human listeners to rate the output quality based on how close they sound compared to the

ground truth sample. The results are shown in Tables 10 and 11. We find A^2SB consistently and significantly outperforms baselines on both tasks and all three test sets. We also find having more partitions consistently improves subjective scores. Especially, the improvements from no partitioning to 2-partitioning are solid, and further increasing the number of partitions to 4 yields diminishing returns. Combining all objective and subjective results, we conclude that *the 4-partitioned A^2SB has the best overall quality*, but *the 2-partitioned A^2SB constitutes a better cost-performance ratio*.

Table 10: Human evaluation results on bandwidth extension.

Method	MOS (bandwidth extension)		
	AAM	CCMixter	MTD
Ground Truth	4.36 ± 0.04	4.39 ± 0.05	4.26 ± 0.04
AudioSR	3.65 ± 0.08	3.67 ± 0.08	3.72 ± 0.10
CQTDiff	3.85 ± 0.08	3.10 ± 0.12	2.99 ± 0.10
IBAR	3.89 ± 0.07	2.96 ± 0.13	3.75 ± 0.07
A^2SB (no partitioning)	4.13 ± 0.06	4.10 ± 0.07	3.79 ± 0.07
A^2SB (2-partitioning)	4.17 ± 0.06	4.17 ± 0.06	3.96 ± 0.06
A^2SB (4-partitioning)	4.18 ± 0.06	4.08 ± 0.06	3.97 ± 0.06

Table 11: Human evaluation results on inpainting.

Method	MOS (inpainting)		
	AAM	CCMixter	MTD
Ground Truth	4.41 ± 0.05	4.36 ± 0.04	4.38 ± 0.05
MAID	3.27 ± 0.10	3.28 ± 0.10	3.33 ± 0.10
CQTDiff	3.59 ± 0.08	3.64 ± 0.09	3.63 ± 0.09
IBAR	3.70 ± 0.08	3.69 ± 0.08	3.96 ± 0.07
A^2SB (no partitioning)	3.96 ± 0.07	3.82 ± 0.08	4.02 ± 0.07
A^2SB (2-partitioning)	4.00 ± 0.07	3.85 ± 0.08	4.09 ± 0.06
A^2SB (4-partitioning)	4.06 ± 0.06	3.92 ± 0.07	4.10 ± 0.06

We then investigate how accurately the objective metrics could predict perceptual quality (MOS). We compute the Spearman Correlation between MOS and each objective metric (–LSD, SiSpec, and ViSQOL) in Table 12. Results indicate all the three objective metrics are moderately correlated with the MOS metric, but far from perfect. ⁶

Table 12: Spearman Correlation between MOS and objective metrics. All p-values are less than 0.001.

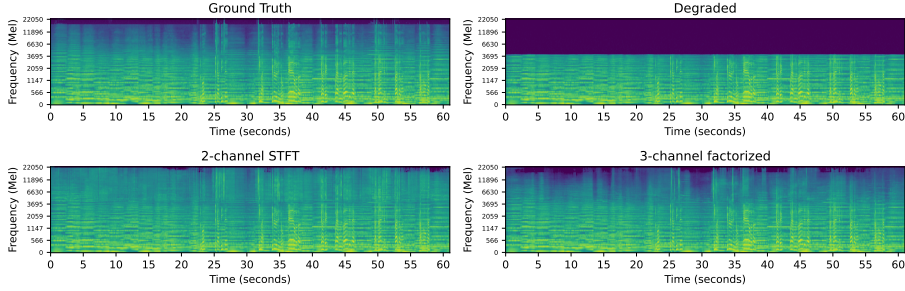
Task	–LSD	SiSpec	ViSQOL
Bandwidth extension (cutoff = 4kHz)	0.443	0.491	0.450
Inpainting (gap = 1000ms)	0.549	0.461	0.480

4.5 NECESSITY OF FACTORIZED AUDIO REPRESENTATION

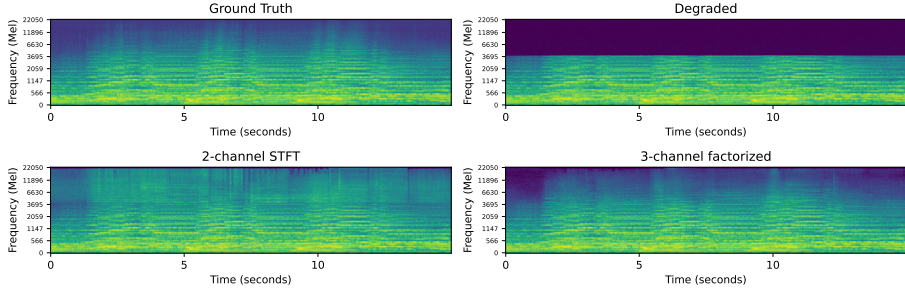
In this section, we demonstrate that compared to the simple complex representation (S in Section 3.1), our three-channel factorized audio representation (7) leads to better fit of the magnitude spectrogram. This thus confirms that factorizing magnitude out from phase and treating them as separate channels prevents the difficulties of modeling phase values from affecting the magnitude modeling task.

In Figure 4, we visualize generated samples of our model trained on STFT and factorized representations, respectively. It is clearly seen that the STFT representation leads to artifacts around the cutoff frequency, while this is alleviated in our factorized audio representation. The overestimation of higher frequency magnitudes is also visible in the 2-channel spectrogram. These results suggest that using the factorized representation is often a better choice and should have more stable learning dynamics.

⁶We additionally fit linear regression between MOS and objective metrics, and obtain the following results. For bandwidth extension, $MOS = 3.2158 - 0.0411 \times LSD + 0.1567 \times \text{sign}(\text{SiSpec}) \times \log |\text{SiSpec}| + 0.1015 \times \text{ViSQOL}$ ($R^2 = 0.311$). For inpainting, $MOS = 4.1775 - 1.4022 \times LSD + 0.0681 \times \text{sign}(\text{SiSpec}) \times \log |\text{SiSpec}| + 0.0649 \times \text{ViSQOL}$ ($R^2 = 0.252$).



(a) Comparing audio representations: sample 1.



(b) Comparing audio representations: sample 2.

Figure 4: Qualitative comparison between A^2SB trained with two-channel STFT representation (S) and our proposed three-channel factorized representation ($\tilde{7}$). The model trained with the two-channel STFT representation has artifacts around the cutoff frequency and predicts too much content for higher frequencies, validating the effectiveness of our three-channel factorized representation.

In Figure 5, we report the average magnitude at different frequency bands. In detail, we randomly select 10 music samples from each test set for this experiment, and report the averaged magnitude over these samples. Results indicate that the complex representation poorly estimates magnitude in all frequency bands. In contrast, our three-channel factorized representation leads to similar magnitude mass compared to ground truth.

4.6 NECESSITY OF PHASE ORTHOGONALIZATION

We study the impact of applying phase orthogonalization in (13), where we find that the model's output are sufficiently close to being proper rotations and require only small adjustments. In Figure 6, we visualize the distribution of the phase orthogonalization error $\text{Err}_{\text{phase-ortho}}(X_{i,j})$ in (18) at different frequency bands. In detail, we consider the bandwidth extension task with cutoff = 4kHz. We take the generated part (above 4kHz) of the output spectrogram and uniformly split it into 9 bins along the frequency axis. We then plot the distribution of $\text{Err}_{\text{phase-ortho}}$ values within each bin.

We note that orthogonalization error is very small (the average error is around the order of 10^{-5}), indicating that our model is able to learn the proposed audio representation very well. Only a small fraction ($< .1\%$) of the spectrogram may have larger phase orthogonalization error (up to 1.5), which will be corrected by phase orthogonalization (13). Overall, the phase orthogonalization provides the necessary guarantee to ensure proper STFT inversion, while likely having nominal impact on perceptual quality given the scale of its adjustments.

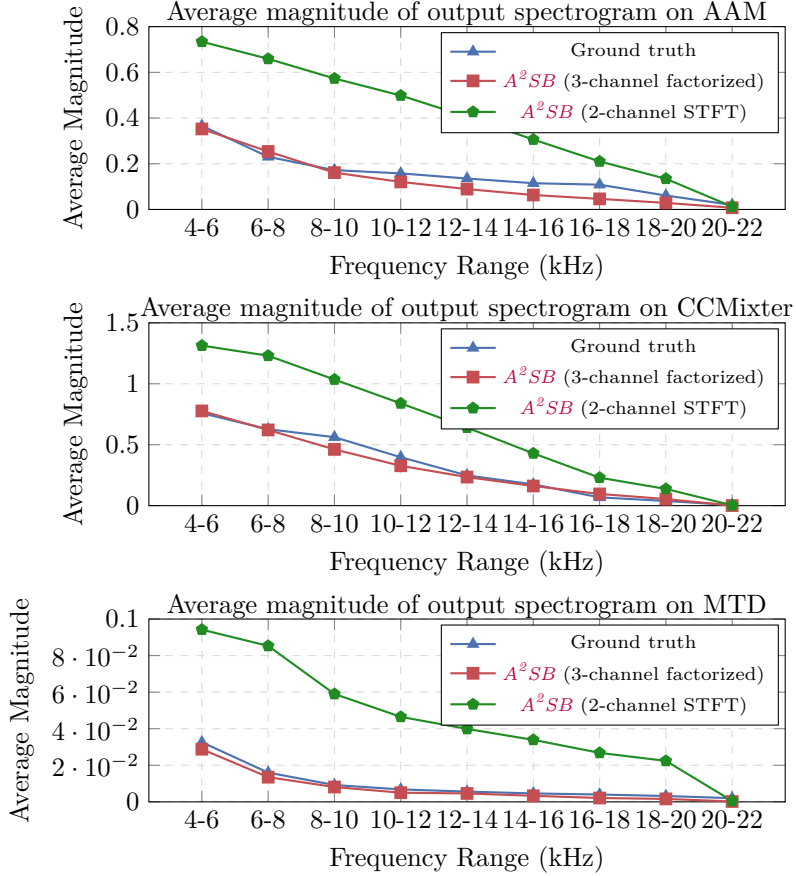


Figure 5: This plot compares the average spectrogram magnitude of outputs from models trained with different audio representations: 2-channel STFT and our proposed 3-channel factorized representation (7). The results in this plot demonstrate that jointly modeling phase and magnitude without uncoupling may result in overall inaccurate magnitude generations compared to that of the target distribution.

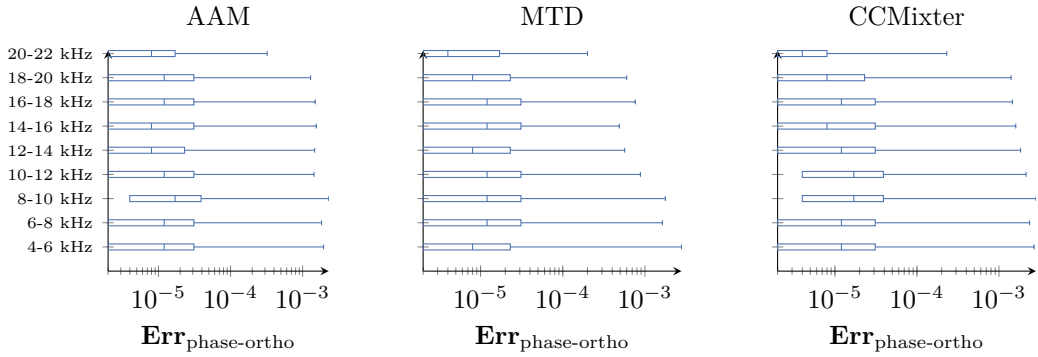


Figure 6: These box-plots visualize the distribution of the (log-scale) phase orthogonalization error $\text{Err}_{\text{phase-ortho}}$ in (18) without any orthogonalization correction. The left-most whisker is omitted and is effectively zero. The right most whisker represents the 99.9-th percentile, where the outlying .01% is omitted from the graph and may have an error of as high as 1.5. The results indicate that our model can predict very accurate trigonometric values of phase for most of the time, and the phase orthogonalization acts primarily as an occasionally necessary safeguard.

4.7 MEMORY USAGE FOR LONG AUDIO RESTORATION

We study the GPU memory usage with MultiDiffusion enabled in our model. We consider the bandwidth extension experiment with a cutoff frequency of 4kHz, and use the no-partitioning model to record GPU memory usage.⁷ We demonstrate the results versus input audio length in Figure 7. The slope shows the memory usage from the cached vector fields in MultiDiffusion, which could be further optimized by moving them to the CPU after computing the vector field for each patch \mathbf{int}_k . The results indicate that our model can up-sample several minutes of audio on a common gaming GPU with ~ 10 G memory and over an hour on a professional GPU with > 50 G memory. We may obtain more memory reduction as well as acceleration by using TensorRT⁸ and custom CUDA kernels⁹.

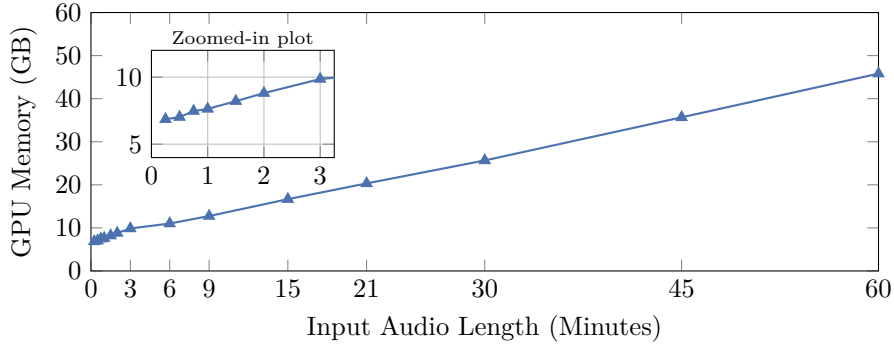


Figure 7: GPU memory usage versus input audio length (in minutes) at inference time with MultiDiffusion enabled. The GPU memory is recorded for the bandwidth extension experiment with a cutoff frequency at 4kHz. The results show that our model can up-sample several minutes of audio on a common gaming GPU and over an hour on a professional GPU.

4.8 THE EFFECT OF SAMPLING STEPS

We study the effect of sampling steps in A^2SB . We conduct this experiment on a subset of the MTD dataset, and consider bandwidth extension with cutoff = 4kHz and inpainting with gap = 1000ms. The model is the 2-partitioning A^2SB . Results are shown in Figures 8 and 9. The results indicate that A^2SB yields almost identical generation quality with different number of sampling steps as low as 25.

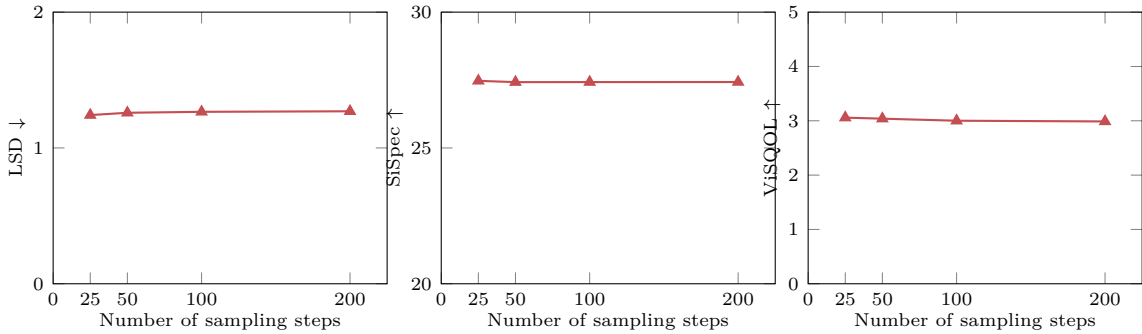


Figure 8: Objective evaluation results with different sampling steps in A^2SB . We evaluate on a subset of MTD with cutoff = 4kHz. Results indicate A^2SB has almost identical quality when we use less sampling steps.

⁷Note that for partitioned models, we could move unused checkpoints to CPU for each t -range.

⁸<https://github.com/NVIDIA/TensorRT>

⁹https://pytorch.org/tutorials/advanced/custom_ops_landing_page.html#custom-ops-landing-page

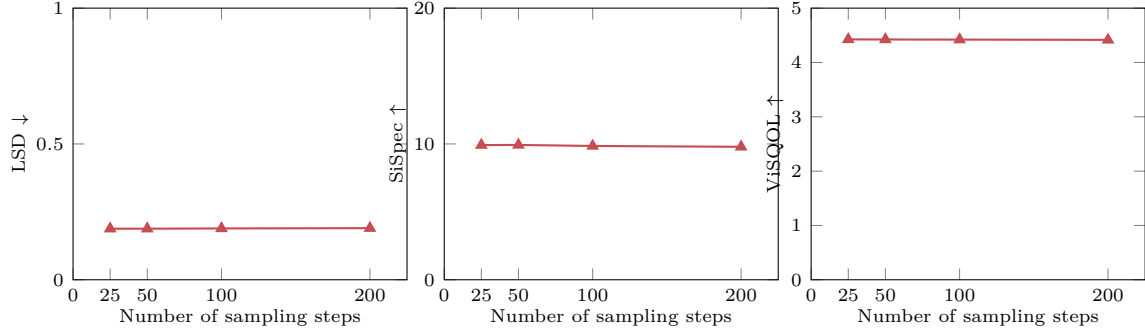


Figure 9: Objective evaluation results with different sampling steps in A^2SB . We evaluate on a subset of MTD with inpainting gap = 1000ms. Results indicate A^2SB has almost identical quality when we use less sampling steps.

5 CONCLUSION AND FUTURE WORK

This paper presents A^2SB , a novel audio restoration model for music bandwidth extension and inpainting at 44.1kHz. We present an end-to-end solution requiring no vocoder or codec. We demonstrate more stable learning dynamics with a factorized magnitude-phase STFT representation, while also guaranteeing proper phase values with SVD orthogonalization. We use a two-stage training strategy and a t -range partitioning method to improve quality, as well as a sampling method for very long audio restoration. We also curated a collection of permissively licensed high quality music data to train our model. Extensive experiments show that A^2SB achieves the state-of-the-art quality on several OOD test sets, validating the effectiveness and generalization ability of our model.

For future works, we plan to: (1) extend A^2SB to support more audio restoration tasks beyond bandwidth extension and inpainting, (2) investigate using the most recent advances in large-scale model architectures to scale-up our model for better quality, generalization, and emergent abilities, (3) investigate better usage of training data in the setup where we combine data from very different data distributions, and (4) extend our solution to stereo music.

ACKNOWLEDGMENTS

We thank Siddharth Gururani and Pin-Jui Ku for helpful discussions at the early stages of this work.

REFERENCES

Andrea Agostinelli, Timo I Denk, Zalán Borsos, Jesse Engel, Mauro Verzetti, Antoine Caillon, Qingqing Huang, Aren Jansen, Adam Roberts, Marco Tagliasacchi, et al. Musiclm: Generating music from text. *arXiv preprint arXiv:2301.11325*, 2023.

Michael S Albergo, Nicholas M Boffi, and Eric Vanden-Eijnden. Stochastic interpolants: A unifying framework for flows and diffusions. *arXiv preprint arXiv:2303.08797*, 2023.

Brian DO Anderson. Reverse-time diffusion equation models. *Stochastic Processes and their Applications*, 12(3):313–326, 1982.

Ihab Asaad, Maxime Jacquelin, Olivier Perrotin, Laurent Girin, and Thomas Hueber. Fill in the gap! combining self-supervised representation learning with neural audio synthesis for speech inpainting. *arXiv preprint arXiv:2405.20101*, 2024.

Yogesh Balaji, Seungjun Nah, Xun Huang, Arash Vahdat, Jiaming Song, Qinsheng Zhang, Karsten Kreis, Miika Aittala, Timo Aila, Samuli Laine, et al. ediff-i: Text-to-image diffusion models with an ensemble of expert denoisers. *arXiv preprint arXiv:2211.01324*, 2022.

Omer Bar-Tal, Lior Yariv, Yaron Lipman, and Tali Dekel. Multidiffusion: Fusing diffusion paths for controlled image generation. *arXiv preprint arXiv:2302.08113*, 2023.

Dmitry Bogdanov, Minz Won, Philip Tovstogan, Alastair Porter, and Xavier Serra. The mtg-jamendo dataset for automatic music tagging. In *Machine Learning for Music Discovery Workshop, International Conference on Machine Learning (ICML 2019)*, Long Beach, CA, United States, 2019. URL <http://hdl.handle.net/10230/42015>.

Zalán Borsos, Matt Sharifi, and Marco Tagliasacchi. Speechpainter: Text-conditioned speech inpainting. *arXiv preprint arXiv:2202.07273*, 2022.

Ricky TQ Chen and Yaron Lipman. Riemannian flow matching on general geometries. *arXiv preprint arXiv:2302.03660*, 2023.

Tianrong Chen, Guan-Horng Liu, and Evangelos A Theodorou. Likelihood training of schrödinger bridge using forward-backward sdes theory. *arXiv preprint arXiv:2110.11291*, 2021.

Michael Chinen, Felicia SC Lim, Jan Skoglund, Nikita Gureev, Feargus O’Gorman, and Andrew Hines. Visqol v3: An open source production ready objective speech and audio metric. In *2020 twelfth international conference on quality of multimedia experience (QoMEX)*, pp. 1–6. IEEE, 2020.

Hyungjin Chung, Jeongsol Kim, Michael T Mccann, Marc L Klasky, and Jong Chul Ye. Diffusion posterior sampling for general noisy inverse problems. *arXiv preprint arXiv:2209.14687*, 2022a.

Hyungjin Chung, Byeongsu Sim, Dohoon Ryu, and Jong Chul Ye. Improving diffusion models for inverse problems using manifold constraints. *Advances in Neural Information Processing Systems*, 35:25683–25696, 2022b.

Valentin De Bortoli, James Thornton, Jeremy Heng, and Arnaud Doucet. Diffusion schrödinger bridge with applications to score-based generative modeling. *Advances in Neural Information Processing Systems*, 34:17695–17709, 2021.

Michaël Defferrard, Kirell Benzi, Pierre Vandergheynst, and Xavier Bresson. Fma: A dataset for music analysis. *arXiv preprint arXiv:1612.01840*, 2016.

Prafulla Dhariwal and Alexander Nichol. Diffusion models beat gans on image synthesis. *Advances in neural information processing systems*, 34:8780–8794, 2021.

Jesse Engel, Cinjon Resnick, Adam Roberts, Sander Dieleman, Mohammad Norouzi, Douglas Eck, and Karen Simonyan. Neural audio synthesis of musical notes with wavenet autoencoders. In *International Conference on Machine Learning*, pp. 1068–1077. PMLR, 2017.

Adoram Erell and Mitch Weintraub. Estimation using log-spectral-distance criterion for noise-robust speech recognition. In *International Conference on Acoustics, Speech, and Signal Processing*, pp. 853–856. IEEE, 1990.

Curtis Hawthorne, Andriy Stasyuk, Adam Roberts, Ian Simon, Cheng-Zhi Anna Huang, Sander Dieleman, Erich Elsen, Jesse Engel, and Douglas Eck. Enabling factorized piano music modeling and generation with the MAESTRO dataset. In *International Conference on Learning Representations*, 2019. URL <https://openreview.net/forum?id=r11YRjC9F7>.

Jonathan Ho, Ajay Jain, and Pieter Abbeel. Denoising diffusion probabilistic models. *Advances in neural information processing systems*, 33:6840–6851, 2020.

Jonathan Ho, Tim Salimans, Alexey Gritsenko, William Chan, Mohammad Norouzi, and David J Fleet. Video diffusion models. *Advances in Neural Information Processing Systems*, 35:8633–8646, 2022.

Ante Jukić, Roman Korostik, Jagadeesh Balam, and Boris Ginsburg. Schrödinger bridge for generative speech enhancement. *arXiv preprint arXiv:2407.16074*, 2024.

Seung-Bin Kim, Sang-Hoon Lee, Ha-Yeong Choi, and Seong-Whan Lee. Audio super-resolution with robust speech representation learning of masked autoencoder. *IEEE/ACM Transactions on Audio, Speech, and Language Processing*, 2024.

Zhifeng Kong, Wei Ping, Jiaji Huang, Kexin Zhao, and Bryan Catanzaro. Diffwave: A versatile diffusion model for audio synthesis. In *International Conference on Learning Representations*, 2021.

Pin-Jui Ku, Alexander H. Liu, Roman Korostik, Sung-Feng Huang, Szu-Wei Fu, and Ante Jukić. Generative speech foundation model pretraining for high-quality speech extraction and restoration, 2024. URL <https://arxiv.org/abs/2409.16117>.

Junhyeok Lee and Seungu Han. Nu-wave: A diffusion probabilistic model for neural audio upsampling. *arXiv preprint arXiv:2104.02321*, 2021.

Sang-gil Lee, Wei Ping, Boris Ginsburg, Bryan Catanzaro, and Sungroh Yoon. Bigvgan: A universal neural vocoder with large-scale training. In *The Eleventh International Conference on Learning Representations*, 2023. URL https://openreview.net/forum?id=iTtGCMDEzS_.

Sang-gil Lee, Zhifeng Kong, Arushi Goel, Sungwon Kim, Rafael Valle, and Bryan Catanzaro. Etta: Elucidating the design space of text-to-audio models. *arXiv preprint arXiv:2412.19351*, 2024.

Jean-Marie Lemercier, Julius Richter, Simon Welker, Eloi Moliner, Vesa Välimäki, and Timo Gerkmann. Diffusion models for audio restoration. *arXiv preprint arXiv:2402.09821*, 2024.

Christian Léonard. A survey of the schrödinger problem and some of its connections with optimal transport. *arXiv preprint arXiv:1308.0215*, 2013.

Jake Levinson, Carlos Esteves, Kefan Chen, Noah Snavely, Angjoo Kanazawa, Afshin Rostamizadeh, and Ameesh Makadia. An analysis of svd for deep rotation estimation. In H. Larochelle, M. Ranzato, R. Hadsell, M.F. Balcan, and H. Lin (eds.), *Advances in Neural Information Processing Systems*, volume 33, pp. 22554–22565. Curran Associates, Inc., 2020.

Chang Li, Zehua Chen, Fan Bao, and Jun Zhu. Bridge-sr: Schrödinger bridge for efficient sr. *arXiv preprint arXiv:2501.07897*, 2025.

Yaron Lipman, Ricky TQ Chen, Heli Ben-Hamu, Maximilian Nickel, and Matt Le. Flow matching for generative modeling. *arXiv preprint arXiv:2210.02747*, 2022.

Guan-Horng Liu, Arash Vahdat, De-An Huang, Evangelos A. Theodorou, Weili Nie, and Anima Anandkumar. I2sb: image-to-image schrödinger bridge. In *Proceedings of the 40th International Conference on Machine Learning*, ICML’23. JMLR.org, 2023a.

Haohe Liu, Qiuqiang Kong, Qiao Tian, Yan Zhao, DeLiang Wang, Chuanzeng Huang, and Yuxuan Wang. Voicefixer: Toward general speech restoration with neural vocoder. *arXiv preprint arXiv:2109.13731*, 2021.

Haohe Liu, Woosung Choi, Xubo Liu, Qiuqiang Kong, Qiao Tian, and DeLiang Wang. Neural vocoder is all you need for speech super-resolution. *arXiv preprint arXiv:2203.14941*, 2022.

Haohe Liu, Ke Chen, Qiao Tian, Wenwu Wang, and Mark D Plumbley. Audiosr: Versatile audio super-resolution at scale. In *ICASSP 2024-2024 IEEE International Conference on Acoustics, Speech and Signal Processing (ICASSP)*, pp. 1076–1080. IEEE, 2024.

Kaiyang Liu, Wendong Gan, and Chenchen Yuan. Maid: A conditional diffusion model for long music audio inpainting. In *ICASSP 2023-2023 IEEE International Conference on Acoustics, Speech and Signal Processing (ICASSP)*, pp. 1–5. IEEE, 2023b.

Antoine Liutkus, Derry Fitzgerald, Zafar Rafii, Bryan Pardo, and Laurent Daudet. Kernel additive models for source separation. *IEEE Transactions on Signal Processing*, 62(16):4298–4310, 2014.

Vincent Lostanlen and Carmine-Emanuele Celli. Deep convolutional networks on the pitch spiral for musical instrument recognition. *arXiv preprint arXiv:1605.06644*, 2016.

Ethan Manilow, Gordon Wichern, Prem Seetharaman, and Jonathan Le Roux. Cutting music source separation some Slakh: A dataset to study the impact of training data quality and quantity. In *Proc. IEEE Workshop on Applications of Signal Processing to Audio and Acoustics (WASPAA)*. IEEE, 2019.

Andrés Marafioti, Nathanaël Perrauidin, Nicki Holighaus, and Piotr Majdak. A context encoder for audio inpainting. *IEEE/ACM Transactions on Audio, Speech, and Language Processing*, 27(12):2362–2372, 2019.

Andrés Marafioti, Piotr Majdak, Nicki Holighaus, and Nathanaël Perrauidin. Gacela: A generative adversarial context encoder for long audio inpainting of music. *IEEE Journal of Selected Topics in Signal Processing*, 15(1):120–131, 2020.

Eloi Moliner and Vesa Välimäki. Behm-gan: Bandwidth extension of historical music using generative adversarial networks. *IEEE/ACM Transactions on Audio, Speech, and Language Processing*, 31:943–956, 2022.

Eloi Moliner and Vesa Välimäki. Diffusion-based audio inpainting. *arXiv preprint arXiv:2305.15266*, 2023.

Eloi Moliner, Jaakko Lehtinen, and Vesa Välimäki. Solving audio inverse problems with a diffusion model. In *ICASSP 2023-2023 IEEE International Conference on Acoustics, Speech and Signal Processing (ICASSP)*, pp. 1–5. IEEE, 2023.

Abdulvahap Mutlu. Music instrument sounds for classification. *Kaggle*, 2024.

Vivek Sivaraman Narayanaswamy, Jayaraman J Thiagarajan, and Andreas Spanias. On the design of deep priors for unsupervised audio restoration. *arXiv preprint arXiv:2104.07161*, 2021.

Fabian Ostermann, Igor Vatolkin, and Martin Ebeling. Aam: a dataset of artificial audio multitracks for diverse music information retrieval tasks. *EURASIP Journal on Audio, Speech, and Music Processing*, 2023(1):13, 2023.

Long Ouyang, Jeffrey Wu, Xu Jiang, Diogo Almeida, Carroll Wainwright, Pamela Mishkin, Chong Zhang, Sandhini Agarwal, Katarina Slama, Alex Ray, et al. Training language models to follow instructions with human feedback. *Advances in neural information processing systems*, 35:27730–27744, 2022.

William Peebles and Saining Xie. Scalable diffusion models with transformers. In *Proceedings of the IEEE/CVF International Conference on Computer Vision*, pp. 4195–4205, 2023.

Tal Peer and Timo Gerkmann. Phase-aware deep speech enhancement: It’s all about the frame length. *JASA Express Letters*, 2(10), 2022.

Adam Polyak, Amit Zohar, Andrew Brown, Andros Tjandra, Animesh Sinha, Ann Lee, Apoorv Vyas, Bowen Shi, Chih-Yao Ma, Ching-Yao Chuang, et al. Movie gen: A cast of media foundation models. *arXiv preprint arXiv:2410.13720*, 2024.

Colin Raffel, Brian McFee, Eric J Humphrey, Justin Salamon, Oriol Nieto, Dawen Liang, and Daniel PW Ellis. *mir_eval*.

Julius Richter, Simon Welker, Jean-Marie Lemercier, Bunlong Lay, and Timo Gerkmann. Speech enhancement and dereverberation with diffusion-based generative models. *IEEE/ACM Trans. on Audio, Speech, and Language Process.*, 31:2351–2364, 2023.

David Roberts. Piano triads wavset. *Kaggle*, 2022.

Robin Rombach, Andreas Blattmann, Dominik Lorenz, Patrick Esser, and Björn Ommer. High-resolution image synthesis with latent diffusion models. In *Proceedings of the IEEE/CVF conference on computer vision and pattern recognition*, pp. 10684–10695, 2022.

Olaf Ronneberger, Philipp Fischer, and Thomas Brox. U-net: Convolutional networks for biomedical image segmentation. In *Medical image computing and computer-assisted intervention–MICCAI 2015: 18th international conference, Munich, Germany, October 5–9, 2015, proceedings, part III 18*, pp. 234–241. Springer, 2015.

Chitwan Saharia, Jonathan Ho, William Chan, Tim Salimans, David J Fleet, and Mohammad Norouzi. Image super-resolution via iterative refinement. *IEEE transactions on pattern analysis and machine intelligence*, 45(4):4713–4726, 2022.

Peter H Schönemann. A generalized solution of the orthogonal procrustes problem. *Psychometrika*, 31(1):1–10, 1966.

Erwin Schrödinger. Sur la théorie relativiste de l'électron et l'interprétation de la mécanique quantique. In *Annales de l'institut Henri Poincaré*, volume 2, pp. 269–310, 1932.

Joan Serrà, Santiago Pascual, Jordi Pons, R Oguz Araz, and Davide Scaini. Universal speech enhancement with score-based diffusion. *arXiv preprint arXiv:2206.03065*, 2022.

Chenhai Shuai, Chaohua Shi, Lu Gan, and Hongqing Liu. mdctgan: Taming transformer-based gan for speech super-resolution with modified dct spectra. *arXiv preprint arXiv:2305.11104*, 2023.

David Snyder, Guoguo Chen, and Daniel Povey. Musan: A music, speech, and noise corpus. *arXiv preprint arXiv:1510.08484*, 2015.

Jascha Sohl-Dickstein, Eric Weiss, Niru Maheswaranathan, and Surya Ganguli. Deep unsupervised learning using nonequilibrium thermodynamics. In *International conference on machine learning*, pp. 2256–2265. PMLR, 2015.

Jiaming Song, Arash Vahdat, Morteza Mardani, and Jan Kautz. Pseudoinverse-guided diffusion models for inverse problems. In *International Conference on Learning Representations*, 2023.

Yang Song, Jascha Sohl-Dickstein, Diederik P Kingma, Abhishek Kumar, Stefano Ermon, and Ben Poole. Score-based generative modeling through stochastic differential equations. In *International Conference on Learning Representations*, 2021.

Bob L Sturm. The gtzan dataset: Its contents, its faults, their effects on evaluation, and its future use. *arXiv preprint arXiv:1306.1461*, 2013.

Jianlin Su, Murtadha Ahmed, Yu Lu, Shengfeng Pan, Wen Bo, and Yunfeng Liu. Roformer: Enhanced transformer with rotary position embedding. *Neurocomputing*, 568:127063, 2024.

John Thickstun, Zaid Harchaoui, and Sham M. Kakade. Learning features of music from scratch. In *International Conference on Learning Representations (ICLR)*, 2017.

Alexander Tong, Nikolay Malkin, Guillaume Huguet, Yanlei Zhang, Jarrid Rector-Brooks, Kilian Fatras, Guy Wolf, and Yoshua Bengio. Conditional flow matching: Simulation-free dynamic optimal transport. *arXiv preprint arXiv:2302.00482*, 2023.

Siyi Wang, Siyi Liu, Andrew Harper, Paul Kendrick, Mathieu Salzmann, and Milos Cernak. Diffusion-based speech enhancement with schrödinger bridge and symmetric noise schedule. *arXiv preprint arXiv:2409.05116*, 2024.

Yuancheng Wang, Zeqian Ju, Xu Tan, Lei He, Zhizheng Wu, Jiang Bian, et al. Audit: Audio editing by following instructions with latent diffusion models. *Advances in Neural Information Processing Systems*, 36:71340–71357, 2023.

Yi-Chiao Wu, Dejan Marković, Steven Krenn, Israel D. Gebru, and Alexander Richard. Scoredec: A phase-preserving high-fidelity audio codec with a generalized score-based diffusion post-filter. In *ICASSP 2024 - 2024 IEEE International Conference on Acoustics, Speech and Signal Processing (ICASSP)*, pp. 361–365, 2024. doi: 10.1109/ICASSP48485.2024.10448371.

Yusong Wu, Ke Chen, Tianyu Zhang, Yuchen Hui, Taylor Berg-Kirkpatrick, and Shlomo Dubnov. Large-scale contrastive language-audio pretraining with feature fusion and keyword-to-caption augmentation. In *ICASSP 2023-2023 IEEE International Conference on Acoustics, Speech and Signal Processing (ICASSP)*, pp. 1–5. IEEE, 2023.

Linting Xue, Aditya Barua, Noah Constant, Rami Al-Rfou, Sharan Narang, Mihir Kale, Adam Roberts, and Colin Raffel. Byt5: Towards a token-free future with pre-trained byte-to-byte models. *Transactions of the Association for Computational Linguistics*, 10:291–306, 2022.

Chin-Yun Yu, Sung-Lin Yeh, György Fazekas, and Hao Tang. Conditioning and sampling in variational diffusion models for speech super-resolution. In *ICASSP 2023-2023 IEEE International Conference on Acoustics, Speech and Signal Processing (ICASSP)*, pp. 1–5. IEEE, 2023.

Jun-Hak Yun, Seung-Bin Kim, and Seong-Whan Lee. Flowhigh: Towards efficient and high-quality audio super-resolution with single-step flow matching. *arXiv preprint arXiv:2501.04926*, 2025.

Frank Zalkow, Stefan Balke, Vlora Arifi-Müller, and Meinard Müller. Mtd: A multimodal dataset of musical themes for mir research. *Trans. Int. Soc. Music. Inf. Retr.*, 3(1):180–192, 2020.

A MORE SAMPLES ON BANDWIDTH EXTENSION

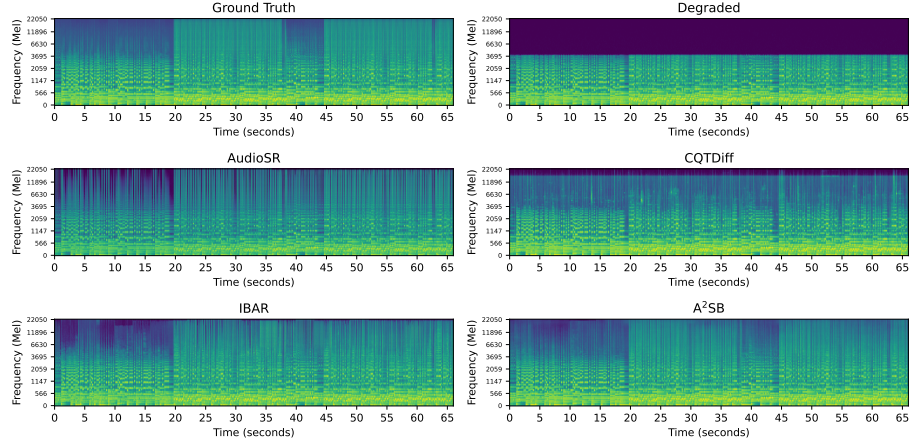


Figure 10: Qualitative comparison between different bandwidth extension methods with cutoff = 4kHz.

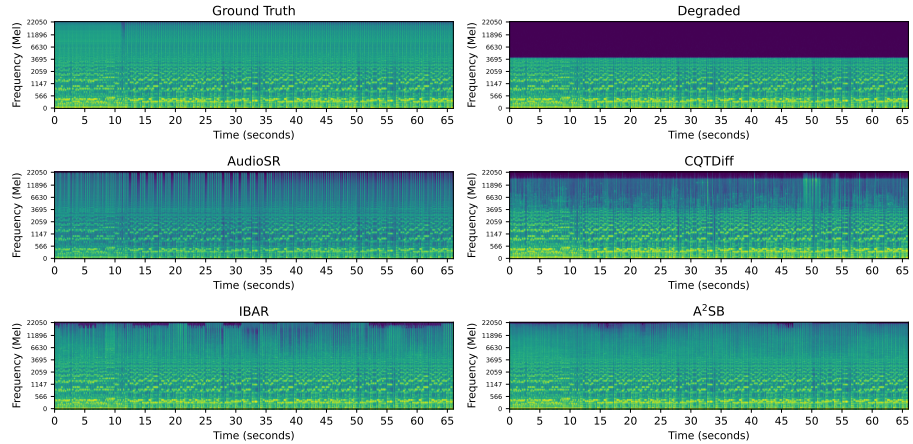


Figure 11: Qualitative comparison between different bandwidth extension methods with cutoff = 4kHz.

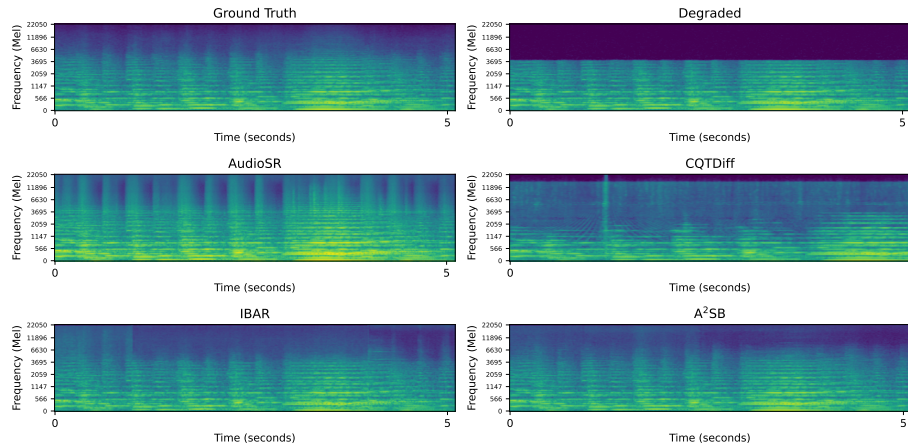


Figure 12: Qualitative comparison between different bandwidth extension methods with cutoff = 4kHz.

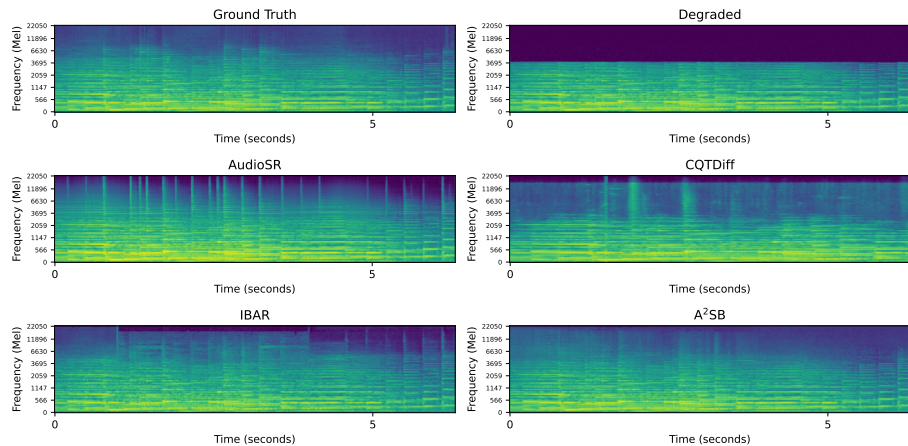


Figure 13: Qualitative comparison between different bandwidth extension methods with cutoff = 4kHz.

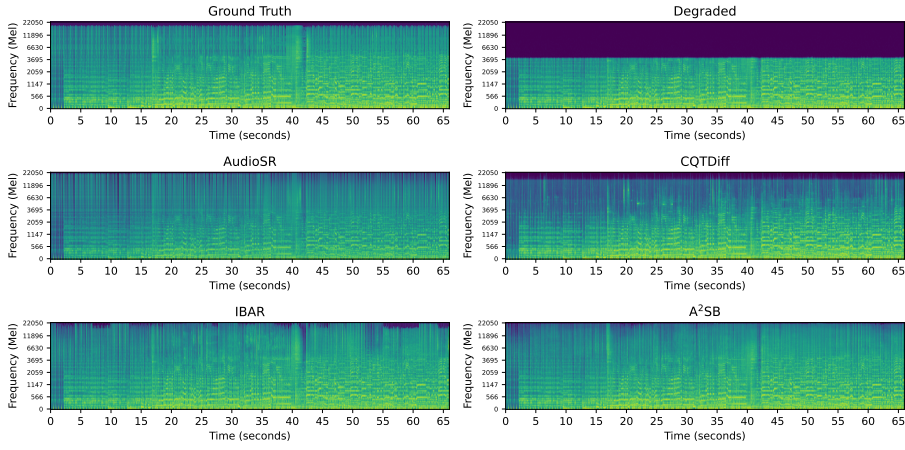


Figure 14: Qualitative comparison between different bandwidth extension methods with cutoff = 4kHz.

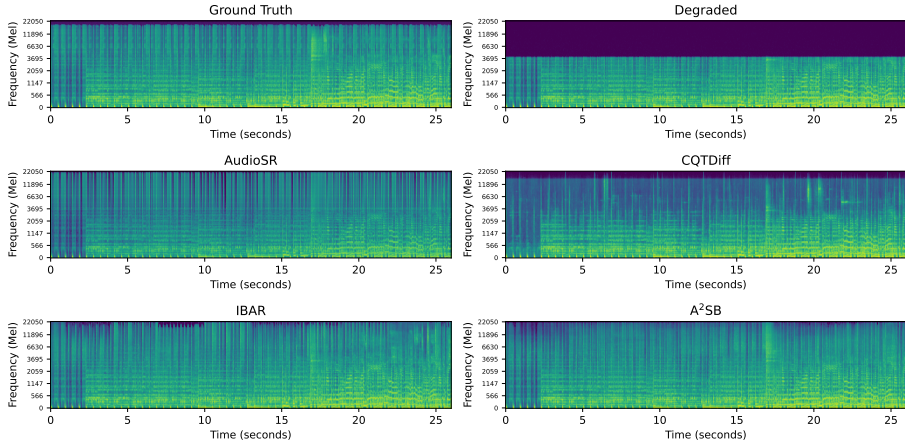


Figure 15: Qualitative comparison between different bandwidth extension methods with cutoff = 4kHz.

B MORE SAMPLES ON INPAINTING

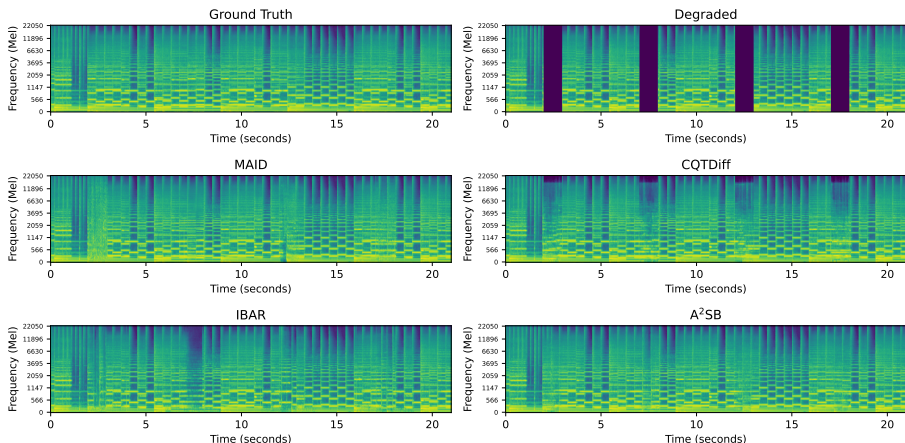


Figure 16: Qualitative comparison between different inpainting methods with inpainting gap = 1 sec.

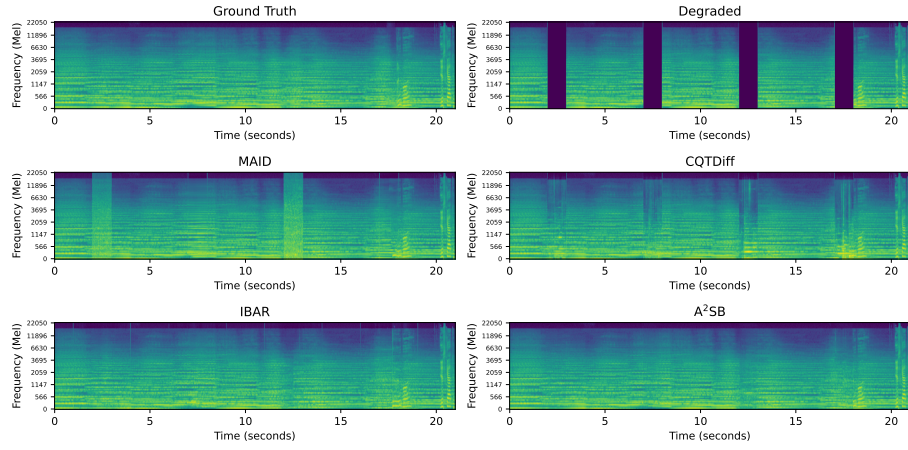


Figure 17: Qualitative comparison between different inpainting methods with inpainting gap = 1 sec.

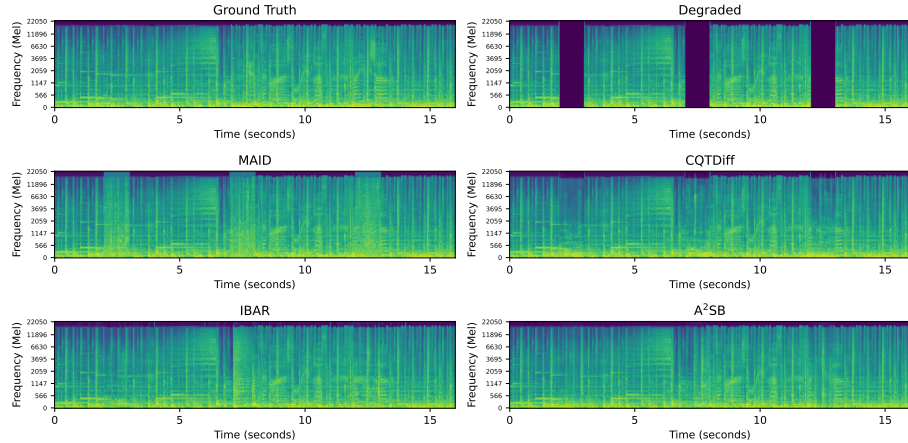


Figure 18: Qualitative comparison between different inpainting methods with inpainting gap = 1 sec.

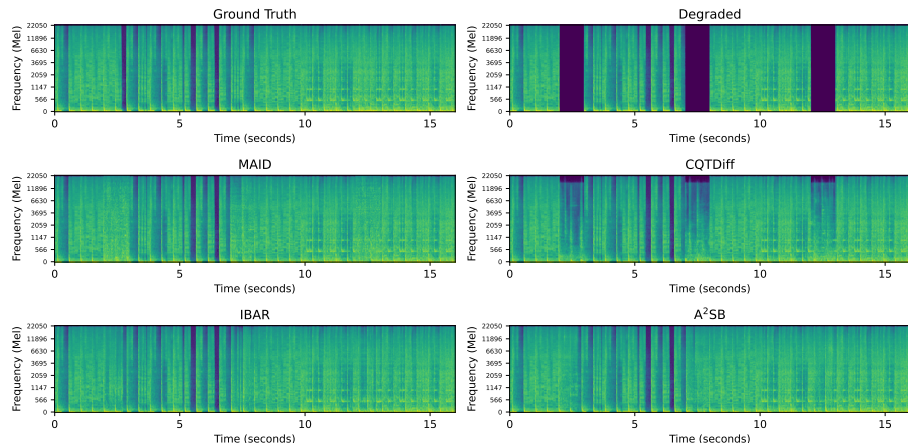


Figure 19: Qualitative comparison between different inpainting methods with inpainting gap = 1 sec.

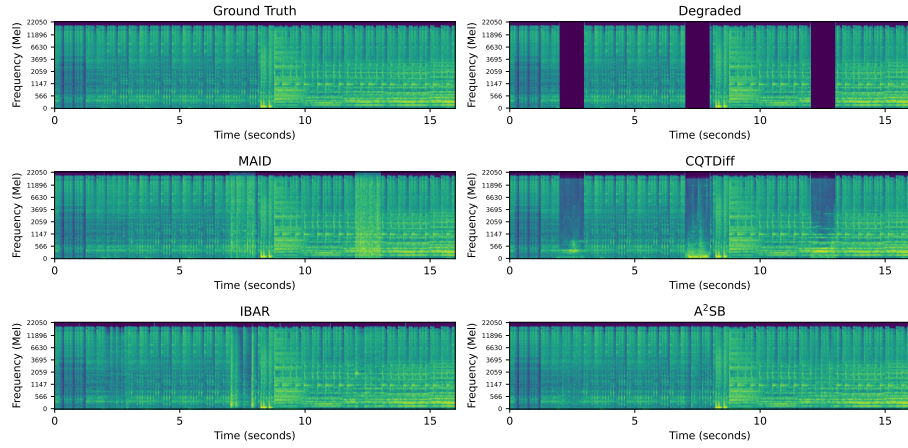


Figure 20: Qualitative comparison between different inpainting methods with inpainting gap = 1 sec.

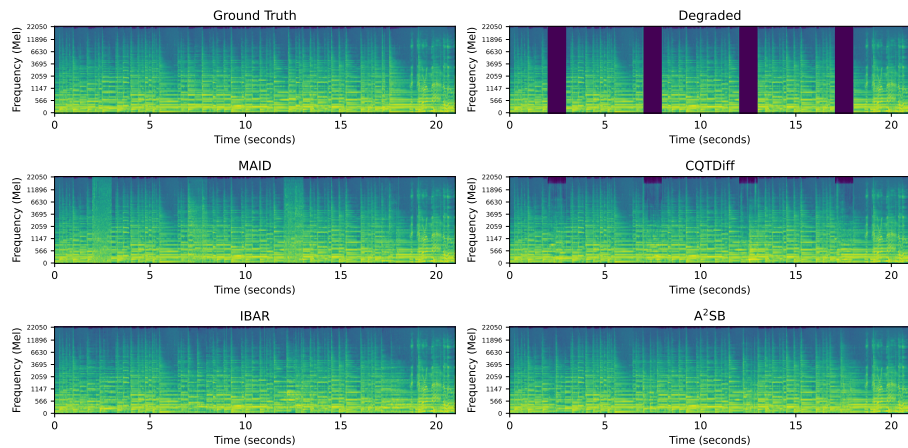


Figure 21: Qualitative comparison between different inpainting methods with inpainting gap = 1 sec.